Publ. Astron. Soc. Japan (2021) 73 (SP1), S172–S200
doi: 10.1093/pasj/psz028
Advance Access Publication Date: 2019 April 21

Massive star formation in W 51 A triggered by cloud–cloud collisions

Shinji FUJITA,[1,2,3,*] Kazufumi TORII,[4] Nario KUNO,[2,3] Atsushi NISHIMURA,[1] Tomofumi UMEMOTO,[4,5] Tetsuhiro MINAMIDANI,[4,5] Mikito KOHNO,[1] Mitsuyoshi YAMAGISHI,[6] Tomoka TOSAKI,[7] Mitsuhiro MATSUO,[8] Yuya TSUDA,[9] Rei ENOKIYA,[1] Kengo TACHIHARA,[1] Akio OHAMA,[1] Hidetoshi SANO,[1] Kazuki OKAWA,[1] Katsuhiro HAYASHI,[1] Satoshi YOSHIIKE,[1] Daichi TSUTSUMI,[1] Yasuo FUKUI,[1] and other FUGIN members

[1]Department of Astrophysics, Nagoya University, Furo-cho, Chikusa-ku, Nagoya, Aichi 464-8602, Japan
[2]Department of Physics, Graduate School of Pure and Applied Sciences, University of Tsukuba, 1-1-1 Tennodai, Tsukuba, Ibaraki 305-8577, Japan
[3]Tomonaga Center for the History of the Universe, University of Tsukuba, 1-1-1 Tennodai, Tsukuba, Ibaraki 305-8571, Japan
[4]Nobeyama Radio Observatory, National Astronomical Observatory of Japan (NAOJ), National Institutes of Natural Sciences (NINS), 462-2 Minamimaki, Minamisaku, Nagano 384-1305, Japan
[5]Department of Astronomical Science, School of Physical Science, SOKENDAI (The Graduate University for Advanced Studies), 2-21-1 Osawa, Mitaka, Tokyo 181-8588, Japan
[6]Institute of Space and Astronautical Science, Japan Aerospace Exploration Agency, Chuo-ku, Sagamihara, Kanagawa 252-5210, Japan
[7]Department of Geoscience, Joetsu University of Education, Joetsu, Niigata, Japan 943-8512
[8]Graduate Schools of Science and Engineering, Kagoshima University, 1-21-35 Korimoto, Kagoshima, Kagoshima 890-0065, Japan
[9]Meisei University, 2-1-1 Hodokubo, Hino, Tokyo 191-0042, Japan

*E-mail: fujita.shinji@a.phys.nagoya-u.ac.jp

Received 2017 October 20; Accepted 2019 February 20

Abstract

W 51 A is one of the most active star-forming regions in the Milky Way, and includes copious amounts of molecular gas with a total mass of $\sim 6 \times 10^5\, M_\odot$. The molecular gas has multiple velocity components over $\sim$20 km s^{-1}, and interactions between these components have been discussed as the mechanism that triggered the massive star formation in W 51 A. In this paper, we report on an observational study of the molecular gas in W 51 A using the new ^{12}CO, ^{13}CO, and C^{18}O ($J = 1$–0) data covering a $1\overset{\circ}{.}4 \times 1\overset{\circ}{.}0$ area of W 51 A obtained with the Nobeyama 45 m telescope at $20''$ resolution. Our CO data resolved four discrete velocity clouds with sizes and masses of $\sim$30 pc and 1.0–1.9 $\times$ $10^5\, M_\odot$ around radial velocities of 50, 56, 60, and 68 km s^{-1}. Toward the central part of the H II region complex G49.5−0.4 in W 51 A, in which the bright stellar clusters IRS 1 and IRS 2 are located, we identified four C^{18}O clumps having sizes of $\sim$1 pc and column densities of higher than 10^{23} cm^{-2}, which are each embedded within the four velocity clouds. These four clumps are concentrated within a small area of 5 pc, but show a complementary distribution on the sky. In the position–velocity diagram, these clumps are connected with each other by bridge features having weak intensities. The high intensity ratios of ^{13}CO ($J = 3$–2)/($J = 1$–0) also indicate that these four clouds are associated with the H II regions, including IRS 1 and IRS 2. We also reveal that, in the other bright H II region complex G49.4−0.3, the 50, 60, and 68 km s^{-1} clouds show a complementary distribution, with two bridge features connecting between the 50 and 60 km s^{-1} clouds and the 60 and 68 km s^{-1} clouds. An isolated compact H II region G49.57−0.27 located ∼15 pc north of G49.5−0.4 also shows a complementary distribution and a bridge feature. The complementary distribution on the sky and the broad bridge feature in the position–velocity diagram suggest collisional interactions among the four velocity clouds in W 51 A. The timescales of the collisions can be estimated to be several 0.1 Myr as crossing times of the collisions, which are consistent with the ages of the H II regions measured from the sizes of the H II regions with the 21 cm continuum data. We discuss a scenario of cloud–cloud collisions and massive star formation in W 51 A by comparing these with recent observational and theoretical studies of cloud–cloud collision.

Key words: ISM: clouds — ISM: individual objects (W 51) — radio lines: ISM — stars: formation

1 Introduction

1.1 W 51

Massive stars are influential in the galactic environment by releasing heavy elements and a large amount of energy in ultraviolet (UV) radiation, stellar winds, outflows, and supernova explosions. It is therefore of fundamental importance to understand the mechanisms of massive star formation, and considerable efforts have been made so far (e.g., Wolfire & Cassinelli 1987; Zinnecker & Yorke 2007; Tan et al. 2014). Since giant molecular clouds (GMCs) are the principal sites of massive star formation (e.g., Zinnecker & Yorke 2007), performing large-scale molecular line observations on GMCs at high spatial resolution is important. A spatial resolution of less than 1 pc allows one to resolve the dense clumps embedded in GMCs, providing crucial information about massive star formation.

W 51 is one of the most active massive star-forming regions in the Milky Way (MW). It was discovered by observations of the thermal radio continuum emission at 21 cm (Westerhout 1958). The distance to W 51 was measured as 5.4 ± 0.3 kpc by Sato et al. (2010) based on observations of trigonometric parallax, and the total far-infrared luminosity of W 51 is as high as ∼8 × 10^6 $L_{\odot}$ at 5.4 kpc (Rengarajan et al. 1984). As shown in figure 1, which shows a two-color composite image of W 51 with the Spitzer 8 and 24 μm data overlaid with a contour map of the 21 cm emission, W 51 consists of a number of H II regions for a large area of ∼1°, which corresponds to ∼100 pc at 5.4 kpc, and these H II regions are separated into two major groups, called W 51 A and W 51 B, in the northeastern and southwestern parts of W 51, respectively (Bieging 1975). The 21 cm radio continuum emission data was taken from the THOR (The H I, OH, Recombination line survey of the Milky Way) archive, which is combined with VLA Galactic Plane Survey (VGPS) data (Stil et al. 2006; Beuther et al. 2016). The total stellar masses included in W 51 A and W 51 B were measured as 1.8 × 10^4 $M_{\odot}$ and 1.4 × 10^4 $M_{\odot}$, respectively (Okumura et al. 2000; Kim et al. 2007). A supernova remnant W 51 C is located in the southeast, and can be traced in the non-thermal radio continuum emission (Koo & Moon 1997a, 1997b). In this study we focus on W 51 A, as it is a young (0.1–1 Myr) massive star-forming region (e.g., Kumar et al. 2004, 2015), providing a unique opportunity to investigate the mechanisms yielding one of the highest star-forming rates in our Galaxy (Okumura et al. 2000).

W 51 A harbors two bright H II region complexes, GAL 049.5−00.4 and GAL 049.4−00.3 (hereafter called "G49.5−0.4" and "G49.4−0.3"), which each include several H II regions within ∼10 pc, as shown in the 21 cm continuum emissions in figure 1b. In G49.5−0.4, 16 H II regions, named G49.5−0.4a–i, were identified (Mehringer 1994). The J, H, K', and Brγ photometric observations by Okumura et al. (2000) identified many O-type and early B-type stars toward these H II regions, as summarized in table 1. The sizes of these H II regions range from ∼0.1 pc to ∼2 pc, and these sizes were used to estimate the ages of these H II regions as 0.1–2.6 Myr (Okumura et al. 2000). The two outstanding radio sources G49.5−0.4e and G49.5−0.4d are also known as W51 IRS 1 and IRS 2 (Wynn-Williams et al. 1974), which each harbor four or five O-type stars and two to four early B-type stars, forming bright stellar clusters at the center of G49.5−0.4. The other sources, G49.5−0.4a, b, c1, f, h, and i, also have multiple O-type/early B-type stars. In addition to these H II regions,

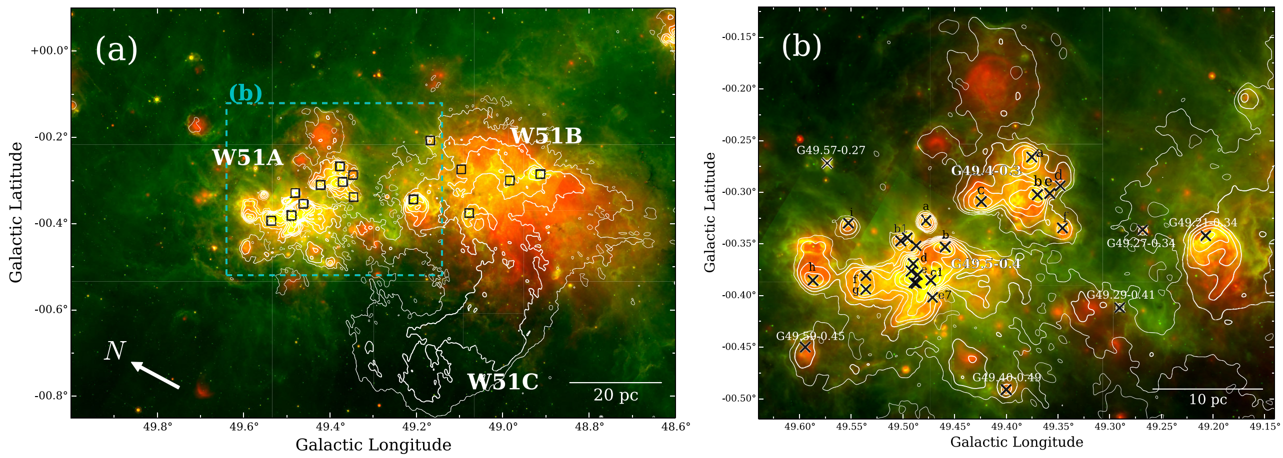

Fig. 1. (a) Composite color image of the Spitzer/MIPSGAL 24 μm (red) and Spitzer/GLIMPSE 8 μm (green) emissions toward W 51. The white contours indicate the THOR 21 cm radio continuum emission combined with the VGPS data (Stil et al. 2006; Beuther et al. 2016), and are plotted from 0.03 (dashed lines) to 3.0 Jy sr^{-1} with logarithmic step. The angular resolution of the combined THOR and VGPS data is 25″. Square symbols represent the compact radio continuum sources identified by Koo (1997). FUGIN data cover the entire region of this map. (b) A close-up view of W 51 A. The corresponding region is indicated by the box with dashed blue lines in panel (a). Crosses represent the H II regions listed in Mehringer (1994)—see also table 1.

many massive young stellar objects (MYSOs) have been identified throughout G49.5−0.4 (Kang et al. 2009; Saral et al. 2017), indicating that massive star formation still continues in this region.

On the other hand, G49.4−0.3 consists of six H II regions, G49.4−0.3a–f, with sizes of ∼0.7–2 pc (Mehringer 1994). Although there is no photometric identification of the exciting stars of these H II regions, their classifications were estimated to be O4–B0, as listed in table 1, from the measurements of ionization photons with the 21 cm radio continuum data (Koo 1997). The typical age of the H II regions was measured as ∼0.2 Myr (see subsection 5.1). Other than G49.5−0.4 and G49.4−0.3, there are several discrete H II regions within ∼20 pc from G49.5−0.4 or G49.4−0.3, and the classifications of the exciting stars in these sources were measured as O4–B0 from the 21 cm data (see the summary in table 1).

Molecular gas in W 51 shows an extended distribution for ∼100 pc × 100 pc, with a total molecular mass measured as ∼7.1 × 10^5 $M_\odot$ at 5.4 kpc (Carpenter & Sanders 1998). The CO emissions in W 51 A have multiple velocity components in a radial velocity (line-of-sight velocity) range of ∼50–70 km s^{-1}. Based on the large-scale ^{12}CO and ^{13}CO (J = 1–0) observations covering the entirety of the W 51 region at an angular resolution of 46″, Carpenter and Sanders (1998) decomposed the velocity structures of the molecular gas by performing fits to the CO spectra with multiple Gaussian functions. Subsequently, Okumura et al. (2001) performed ^{13}CO (J = 1–0) observations at a high angular resolution of 15″ toward a ∼15′ × 15′ area centered on G49.5−0.4. By analyzing the position–velocity diagrams, the authors identified four velocity components around radial velocities of 50, 56, 60, and 68 km s^{-1}.

The 68 km s^{-1} cloud corresponds to the High Velocity Stream (HVS), which is a filamentary molecular cloud stretched nearly parallel to the Galactic plane, overlapping W 51 A and W 51 B along the line of sight. The length and width of HVS were measured as ∼100 pc and ∼10 pc, respectively (Carpenter & Sanders 1998; Kang et al. 2010; Parsons et al. 2012). Burton and Shane (1970) and Koo (1999) discussed the large velocity of HVS as being attributed to the streaming motion of gas down to the Sagittarius spiral arm driven by the spiral density wave. For the velocity components other than HVS, Carpenter and Sanders (1998) discussed that these represent kinematic structures within a single molecular cloud, the W 51 cloud, with a total molecular mass of ∼6.0 × 10^5 $M_\odot$, referred to as the W 51 cloud, whereas Okumura et al. (2001) postulated that these are discrete molecular clouds located at the same distance.

It has been actively debated that the massive star formation in W 51 A was triggered by collisions between molecular clouds having different radial velocities over ∼20 km s^{-1} (Pankonin et al. 1979; Arnal & Goss 1985; Carpenter & Sanders 1998; Koo 1999; Okumura et al. 2001). Carpenter and Sanders (1998) proposed a collision between the W 51 cloud and HVS. The authors revealed that the CO emissions around 60 km s^{-1} in the W 51 cloud truncate at the location of HVS, and discussed these two velocity components as being physically related objects at a common distance, suggesting a collision between these two clouds. Kang et al. (2010) reached the same

Table 1. List of the H II regions and massive stars in W 51 A.*

Name (1)	Radius (pc) (2)	log N_i (photons s^{-1}) (3)	Classification (4)	Age (Myr) (5)	References (6)
G49.21−0.34	4.9	49.8	[O4]	2.2†	[1]
G49.27−0.34	0.9	45.6	[B0]	1.3†	[1]
G49.29−0.41	—	47.3	[B0]	—	[1]
G49.4−0.3 a	1.6	49.0	[O6]	0.5†	[1, 2]
G49.4−0.3 b	0.4	49.7	[O5]	0.1†	[1, 2]
G49.4−0.3 c	1.6	49.3	[O5.5]	0.4†	[1, 2]
G49.4−0.3 d	1.6	48.6	[O7]	0.6†	[1, 2]
G49.4−0.3 e	0.3	47.7	[O9.5]	0.1†	[1, 2]
G49.4−0.3 f	1.6	48.2	[O8.5]	0.8†	[1]
G49.40−0.49	1.3	48.2	[O8.5]	0.5†	[1]
G49.5−0.4 a	1.6	49.0	O5+B1	0.7	[1, 2, 3]
G49.5−0.4 b	1.6	49.6	O4+O8+B0	2.2	[1, 2, 3]
G49.5−0.4 b1	0.7	48.2	O9	0.8	[1, 3]
G49.5−0.4 b2	0.5	47.3	B1	0.2	[1, 3]
G49.5−0.4 b3	0.5	48.1	[O9]	—	[1]
G49.5−0.4 c1	—	49.2	O5+O6+B0	0.4	[1, 3]
G49.5−0.4 d (IRS 2)	1.1	49.7	O4+O6× 4 +B0+B1×3	0.1	[1, 3]
G49.5−0.4 e (IRS 1)	0.4	50.4	O4+O5+O6+O8+B0×2	—	[1, 2, 3]
G49.5−0.4 e1	—	47.9	[O9.5]	—	[1]
G49.5−0.4 e2	—	>47.6	[>B0]	—	[1]
G49.5−0.4 e6	—	47.3	[B0]	—	[1]
G49.5−0.4 e7	—	47.2	B0	0.3	[1, 3]
G49.5−0.4 f	1.9 (f+g)	49.1	O7+B0+B1×2	1.8	[1, 2, 3]
G49.5−0.4 g	1.9 (f+g)	48.9	[O5× 2 +B1]	1.5	[2]
G49.5−0.4 h	3.2	48.9	O5+B0× 4 +B1	2.6	[1, 2, 3]
G49.5−0.4 i	1.6	48.4	O8+B1	1.5	[1, 3]
G49.57−0.27	1.2	47.5	[B0]	0.7†	[1]
G49.59−0.45	3.3	48.7	[O7]	2.1†	[1]

* (1) Name of the H II region. (2) Radius of the H II region taken from the website of the Wide-field Infrared Survey Explorer (WISE) catalog of Galactic H II regions (Anderson et al. 2014; Makai et al. 2017). (3) Ionizing photon flux estimated by Mehringer (1994). (4) Classification of the exciting stars in the H II region estimated by Mehringer (1994) and Okumura et al. (2000). Those derived by measuring ionizing photons from radio continuum image are shown with brackets, while those identified in the near-infrared photometric observations are presented without brackets. (5) Expansion age of the H II region estimated by Okumura et al. (2000) or in this study. Those marked with † were measured in this study (see subsection 4.1). (6) References: [1] Mehringer (1994), [2] Koo (1997), [3] Okumura et al. (2000).

conclusion, based on ^{12}CO and ^{13}CO ($J = 2$–1) observations at 36″ resolution, which covered a 1.°25 × 1.°00 area of W 51. Okumura et al. (2001) argued that a "pileup" scenario of the four discrete molecular clouds resulted in a burst of massive star formation in G49.5−0.4 in W 51 A.

Recently, supersonic collision between molecular clouds has been discussed as a plausible mechanism of massive star formation. These observational studies of cloud–cloud collisions (CCCs) include the super star clusters and the H II regions in the MW and young O stars in the Large Magellanic Cloud (Furukawa et al. 2009; Ohama et al. 2010, 2018a, 2018b; Torii et al. 2011, 2015, 2018, 2021; Shimoikura et al. 2013; Fukui et al. 2014, 2015, 2018a, 2018b; Tsuboi et al. 2015; Nishimura et al. 2017, 2018; Sano et al. 2017; Fujita et al. 2021; Hayashi et al. 2018; Kohno et al. 2018; Takahira et al. 2018), where the super star clusters include 10–20 O stars, while the others include a single young O star. Formation of the massive clumps, which may form massive stars, in the collisional-compressed layer was discussed in depth in the magnetohydrodynamical (MHD) simulations by Inoue and Fukui (2013) and Inoue et al. (2017). Kobayashi et al. (2018) formulated the time evolution equation of the GMC mass function including CCC, indicating that CCC-driven star formation is mostly driven by massive GMCs having masses > $10^{5.5}$ $M_\odot$, which may account for a few tens of percent of the total star formation in the MW and nearby galaxies. Comparisons between the observations and numerical calculations have indicated two important observational signatures of CCCs, i.e., a "broad bridge feature" in position–velocity diagrams and "complementary distribution" on the sky between two molecular clouds with different velocities, which provide useful diagnostics to investigate CCCs with molecular line observations (Habe & Ohta 1992; Anathpindika 2010; Takahira et al. 2014; Torii et al. 2018; Fukui et al. 2018a).

1.2 Observational signatures of CCCs

Based on comparisons between observations and simulations, Fukui et al. (2018a) and Torii et al. (2018) discussed two possible observational signatures of CCCs: a "broad bridge feature" in position–velocity diagrams and "complementary distribution" on the sky between two clouds with different velocities, where the authors assumed a collision between two dissimilar clouds based on the basic CCC scenarios studied by Habe and Ohta (1992), followed by Anathpindika (2010), Takahira, Tasker, and Habe (2014), Haworth et al. (2015a, 2015b), and Takahira et al. (2018). A broad bridge feature is relatively weak CO emissions at intermediate velocities between two colliding clouds that are separated in velocity. When a smaller cloud drives into a larger cloud, a dense compressed layer at the collisional interface is formed, resulting in a thin turbulent layer between the larger cloud and the compressed layer. If one observes a snapshot of this collision with a viewing angle parallel to the colliding axis, two velocity peaks separated by intermediate-velocity emission with lower intensity can be seen in the position–velocity diagrams. The turbulent gas which creates the broad bridge feature can be replenished as long as the collision continues. Several observational studies have reported detections of broad bridge features in CCC regions (e.g., Furukawa et al. 2009; Ohama et al. 2010; Fukui et al. 2014, 2016, 2017; Torii et al. 2015, 2018).

When two clouds collide, one creates a cavity in the other owing to momentum conservation (Haworth et al. 2015a). If the collision takes place head-on between two dissimilar clouds, a cavity will be formed on the larger cloud through this process, and the larger cloud can be seen as a ring-like structure on the sky, unless the observer viewing angle is perfectly perpendicular to the colliding axis. As the size of the cavity corresponds to that of the smaller cloud, the observer with a viewing angle parallel to the colliding axis sees a complementary distribution between the smaller cloud and the ring-like structure of the larger cloud. If the collision is an offset collision, not a head-on collision, the basic process is not changed, and two clouds with different velocities can be observed close to each other. These two clouds may share the boundaries of the clouds on the sky, showing a complementary distribution. Fukui et al. (2018a, 2018b) pointed out that if the observer viewing angle has an inclination relative to the colliding axis, the complementary distribution has a spatial offset depending on the travel distance of the collision or the depth of the cavity.

In well-resolved CCC regions, a combination of the two signatures of CCC, the broad bridge feature and complementary distribution, may be observed as a "V-shaped" gas distribution in the p–v diagram (e.g., Fukui et al. 2018a; Ohama et al. 2018b; Hayashi et al. 2018; Torii et al. 2021). Analyses of synthetic CO data by Fukui et al. (2018a) indicated that, if the observer viewing angle is inclined relative to the colliding axis, the V-shaped distribution becomes skewed.

1.3 Overview of this paper

Following the recent improvement of our knowledge of CCCs as triggers of massive star formation, in this study we present an analysis of new ^{12}CO, ^{13}CO, and C^{18}O (J = 1–0) data covering the entirety of W 51 A in order to test CCC scenarios as the mechanism of the active massive star formation in W 51 A. The CO data was obtained using the Nobeyama 45 m telescope at 20″ resolution, which corresponds to ∼0.5 pc at 5.4 kpc, as part of the Galactic plane survey legacy project FUGIN (FOREST Unbiased Galactic plane Imaging survey with the Nobeyama 45 m telescope: Minamidani et al. 2016; Umemoto et al. 2017). The advantages of our new CO (J = 1–0) data can be summarized as follows:

(1) We covered a large area of 1.°4 × 1.°0, including W 51 A, at a spatial resolution comparable with that in the ^{13}CO (J = 1–0) observations by Okumura et al. (2001), which covered a ∼15′ × 15′ area of G49.5−0.4.

(2) Our data includes the C^{18}O (J = 1–0) emission, which allows us to diagnose the signatures of CCCs in the molecular clouds in W 51 A. Note that C^{18}O (J = 1–0) emission has not been studied for a large area of W 51 A at such a high angular resolution. Parsons et al. (2012) performed large-scale ^{12}CO, ^{13}CO, and C^{18}O (J = 3–2) observations with the James Clerk Maxwell Telescope (JCMT) toward W 51 A and W 51 B, providing a comprehensive catalog of the dense gas in the molecular clouds in W 51 A. However, the authors did not focus on the spatial and velocity distributions of the gas with the aim of investigating interactions among different velocity components.

(3) Our CO data has a spatial resolution comparable with the JCMT archival CO (J = 3–2) data (Parsons et al. 2012), allowing us to investigate the excitation conditions of the gas, and to probe the interaction between molecular gas and H II regions.

Table 2. Summary of the CO (J = 1–0) dataset.

Observation date	2014 March–May and 2015 April–May
Observed area	$l = 50\overset{\circ}{.}0$–$48\overset{\circ}{.}6$, $b = -0\overset{\circ}{.}9$–$+0\overset{\circ}{.}1$ ($1\overset{\circ}{.}4 \times 1\overset{\circ}{.}0$)
Telescope	NRO 45 m telescope
Receiver	FOREST
Observation mode	On-The-Fly
Emission lines	^{12}CO (J = 1–0), ^{13}CO (J = 1–0), and C^{18}O (J = 1–0)
Angular and velocity resolution	∼20″ (∼0.5 pc for a distance of 5.4 kpc) and ∼1.3 km s^{-1}
Angular and velocity grid of the final cube data	8″.5 and 0.65 km s^{-1}
$T_{\rm rms}$	∼1.5 K for ^{12}CO (J = 1–0)
	∼0.7 K for ^{13}CO (J = 1–0)
	∼ 0.7 K for C^{18}O (J = 1–0)

In section 2 we describe the CO dataset used in this study, and in section 3 we present the main results of the analyses on the CO dataset and comparisons with the other wavelengths. In section 4 we discuss the results, and we present a summary in section 5.

2 Dataset

The observations of W 51 A were carried out as a part of the FUGIN project (Umemoto et al. 2017) with the Nobeyama Radio Observatory (NRO) 45 m telescope. Details of the observations, calibration, and data reduction are summarized in Umemoto et al. (2017), and parameters of the observations and output data are listed in table 2. In W 51 A, we covered an area of $l = 50\overset{\circ}{.}0$–$48\overset{\circ}{.}6$, $b = -0\overset{\circ}{.}9$–$+0\overset{\circ}{.}1$ ($1\overset{\circ}{.}4 \times 1\overset{\circ}{.}0$) in ^{12}CO ($J$ = 1–0), ^{13}CO (J = 1–0), and C^{18}O (J = 1–0) emissions. The beam size of the NRO 45 m telescope is ∼15″ at 115 GHz, and the effective angular resolution of this mapping is ∼20″. The SAM45 (Spectral Analysis Machine for the 45 m telescope) spectrometer (Kuno et al. 2011) was used at a frequency resolution of 244.14 kHz, and the effective velocity resolution was 1.3 km s^{-1} at 115 GHz. The typical system noise temperatures including atmosphere were ∼150 K and ∼250 K at 110 GHz and 115 GHz, respectively. The output cube data has spatial grids of 8″.5 × 8″.5 and a velocity grid of 0.65 km s^{-1} for the ^{12}CO (J = 1–0), ^{13}CO (J = 1–0), and C^{18}O (J = 1–0) emissions. The final rms noise temperature $T_{\rm rms}$ in the $T_{\rm mb}$ scale are 1.5 K, 0.7 K, and 0.7 K per velocity channel for ^{12}CO (J = 1–0), ^{13}CO (J = 1–0), and C^{18}O (J = 1–0), respectively.

The ^{12}CO (J = 3–2), ^{13}CO (J = 3–2), and C^{18}O (J = 3–2) data were obtained by Parsons et al. (2012) with the Heterodyne Array Receiver Programme (HARP) receiver and the Auto-Correlation Spectral Imaging System (ACSIS) back-end digital autocorrelator spectrometer on the JCMT. The observations covered a $1\overset{\circ}{.}4 \times 1\overset{\circ}{.}0$ area including W 51 A and W 51 B. The data have an angular resolution of 14″ and a velocity resolution of 0.5 km s^{-1}.

In the figures in this paper, to improve the signal-to-noise ratio and compare the FUGIN data with the JCMT data at the same angular resolution, we convolved the dataset with Gaussians of FWHM 22″.4 and 26″.5 for the FUGIN data and the JCMT data, respectively (giving smoothed angular resolutions of $\sqrt{20.0^2 + 22.4^2} \approx$ 30″.0 and $\sqrt{14.0^2 + 26.5^2} \approx$ 30″.0). We also convolved the dataset for the velocity axis to a resolution of 1.3 km s^{-1} using the same method.

3 Results

3.1 Large-scale gas distribution

3.1.1 CO (J = 1–0) distribution

Figures 2a–2d show integrated intensity maps of the ^{12}CO (J = 1–0), ^{13}CO (J = 1–0), C^{18}O (J = 1–0), and ^{13}CO (J = 3–2) emissions integrated over 40–80 km s^{-1}, which covers the W 51 A region shown in figure 1b. In figure 2a the ^{12}CO (J = 1–0) emissions show extended gas distributions over the entire map, while the ^{13}CO (J = 1–0) emissions presented in figure 2b show somewhat clumpy structures. In figure 2c, the C^{18}O (J = 1–0) emissions show more clumpy structures than the ^{13}CO (J = 1–0) emissions. They are strongly detected in G49.5−0.4, indicating the presence of high-density gas in this region. The distribution of ^{13}CO (J = 3–2) emissions (JCMT data obtained by Parsons et al. 2012) presented in figure 2d resembles that of the ^{13}CO (J = 1–0) emissions, but the intensity is relatively low in the northwestern part of the map.

Figures 3a–3d show the spectra of ^{12}CO (J = 1–0), ^{13}CO (J = 1–0), C^{18}O (J = 1–0) (FUGIN data), ^{12}CO (J = 3–2), ^{13}CO (J = 3–2), and C^{18}O (J = 3–2) (JCMT data) toward four representative positions. Figure 3a shows the spectra at the ^{13}CO (J = 1–0) peak positions in G49.5−0.4. CO emissions are detected in the velocity ranges of 45–65 km s^{-1} and ∼68 km s^{-1} with complicated spectral profiles. Figure 3b shows the spectra at the ^{13}CO (J = 1–0) peak positions in G49.4−0.3. The profiles of the spectra have

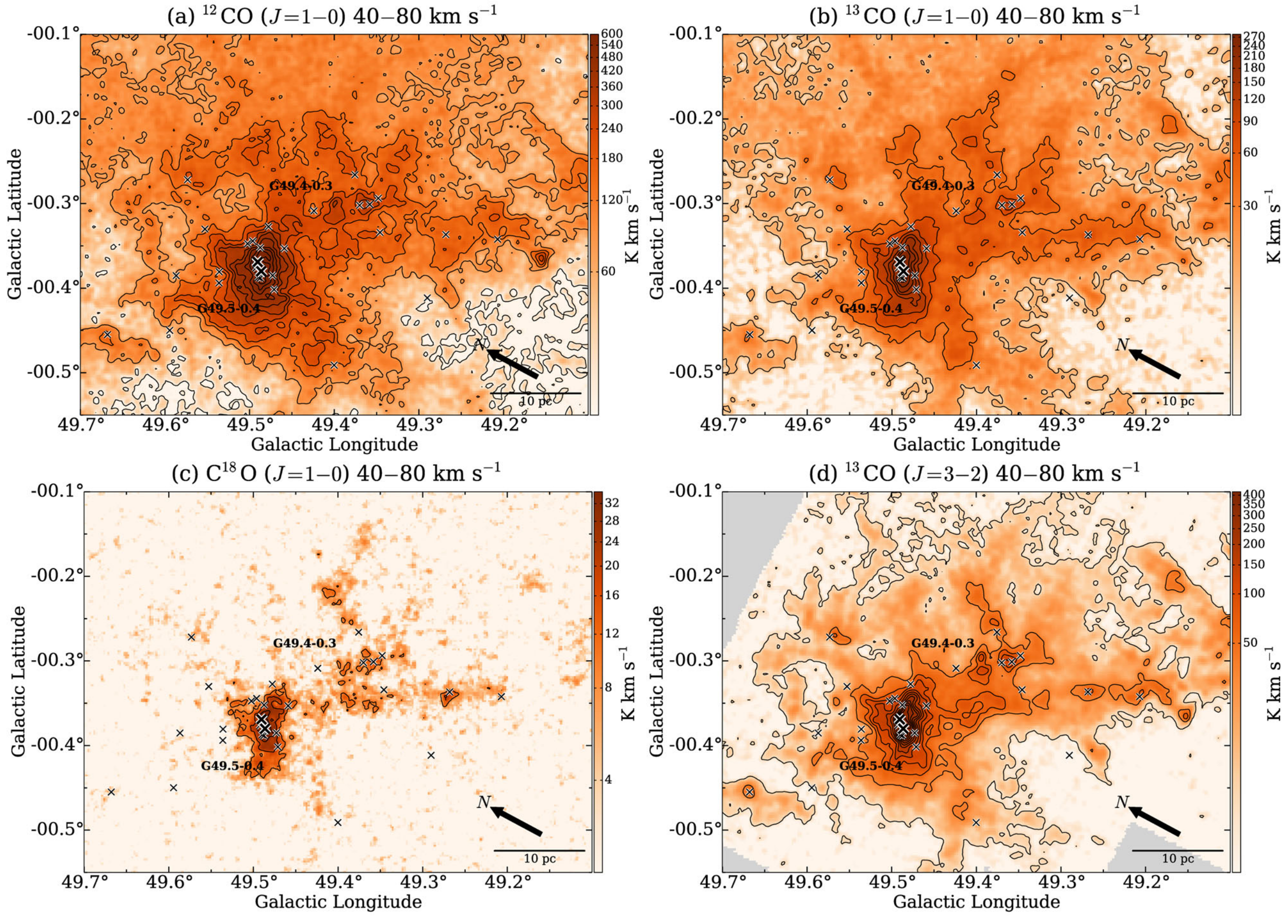

Fig. 2. Integrated intensity map of (a) ^{12}CO (J = 1–0), (b) ^{13}CO (J = 1–0), (c) C^{18}O (J = 1–0), and (d) ^{13}CO (J = 3–2) integrated over 40–80 km s^{-1} toward W 51 A. These maps are colored in a logarithmic scale. The contours are plotted with (a) 9σ (60 K km s^{-1}) intervals starting from the 3σ (20 K km s^{-1}) level, (b) 9σ (30 K km s^{-1}) intervals starting from the 3σ (10K km s^{-1}) level, (c) 3σ (10 K km s^{-1}) intervals starting from the 3σ (10 K km s^{-1}) level, and (d) 2σ (30 K km s^{-1}) intervals starting from the 3σ (50 K km s^{-1}) level, respectively. The gray pixels in (d) indicates the area not covered by JCMT (Parsons et al. 2012).

peaks at ∼51 km s^{-1}, while weak CO emissions are detected around ∼60 km s^{-1}. The CO emissions at ∼68 km s^{-1} seen toward G49.4−0.3 are barely detected. Figures 3c and 3d show the spectra toward the H II regions G49.57−0.27 and G49.34−0.21, respectively. CO emissions are detected in several velocity ranges. In addition, in figure 3d we can see that the ^{12}CO (J = 1–0) and ^{12}CO (J = 3–2) spectra show self-absorption features at ∼66–68 km s^{-1} indicated by the C^{18}O emissions at the velocity.

Figures 4a–4d show the l–v diagrams (integrated along the Galactic latitude over $b = -0\overset{\circ}{.}55$–$-0\overset{\circ}{.}10$) and the v–b diagrams (integrated along the Galactic longitude over $l = 49\overset{\circ}{.}70$–$49\overset{\circ}{.}10$) of the ^{13}CO ($J$ = 1–0) emissions and the ^{13}CO (J = 3–2) emissions. Four discrete velocity components identified in the previous studies (Okumura et al. 2001) can be seen in the spectra, l–v diagram, and v–b diagram, and these clouds are connected with each other by the intermediate velocity emissions. Following the nomenclature of Okumura et al. (2001), we hereafter refer to the velocity components around 50, 56, 60, and 68 km s^{-1} as "the 50 km s^{-1} cloud," "the 56 km s^{-1} cloud," "the 60 km s^{-1} cloud," and "the 68 km s^{-1} cloud (HVS)," respectively.

Besides these four clouds, we can see a molecular cloud near G49.5−0.4 at a higher velocity range (71.6–74.8 km s^{-1}) in the velocity channel maps of the ^{12}CO (J = 1–0) and ^{13}CO (J = 1–0) emissions (figure 19 in appendix 1). It extends perpendicular to the elongation of the 68 km s^{-1} cloud (HVS) down to $b \approx -0\overset{\circ}{.}5$. Its elongation is perhaps related to feedback of the massive stars in G49.5−0.4. In this paper, we disregard the molecular clouds in this velocity range because their CO emission intensity is significantly lower than the other four velocity components.

Figures 5–7 show the ^{12}CO, ^{13}CO, and C^{18}O (J = 1–0) integrated intensity distributions of the four velocity clouds, respectively, overlaid with a contour map of the 21 cm radio continuum data (Stil et al. 2006). We also present

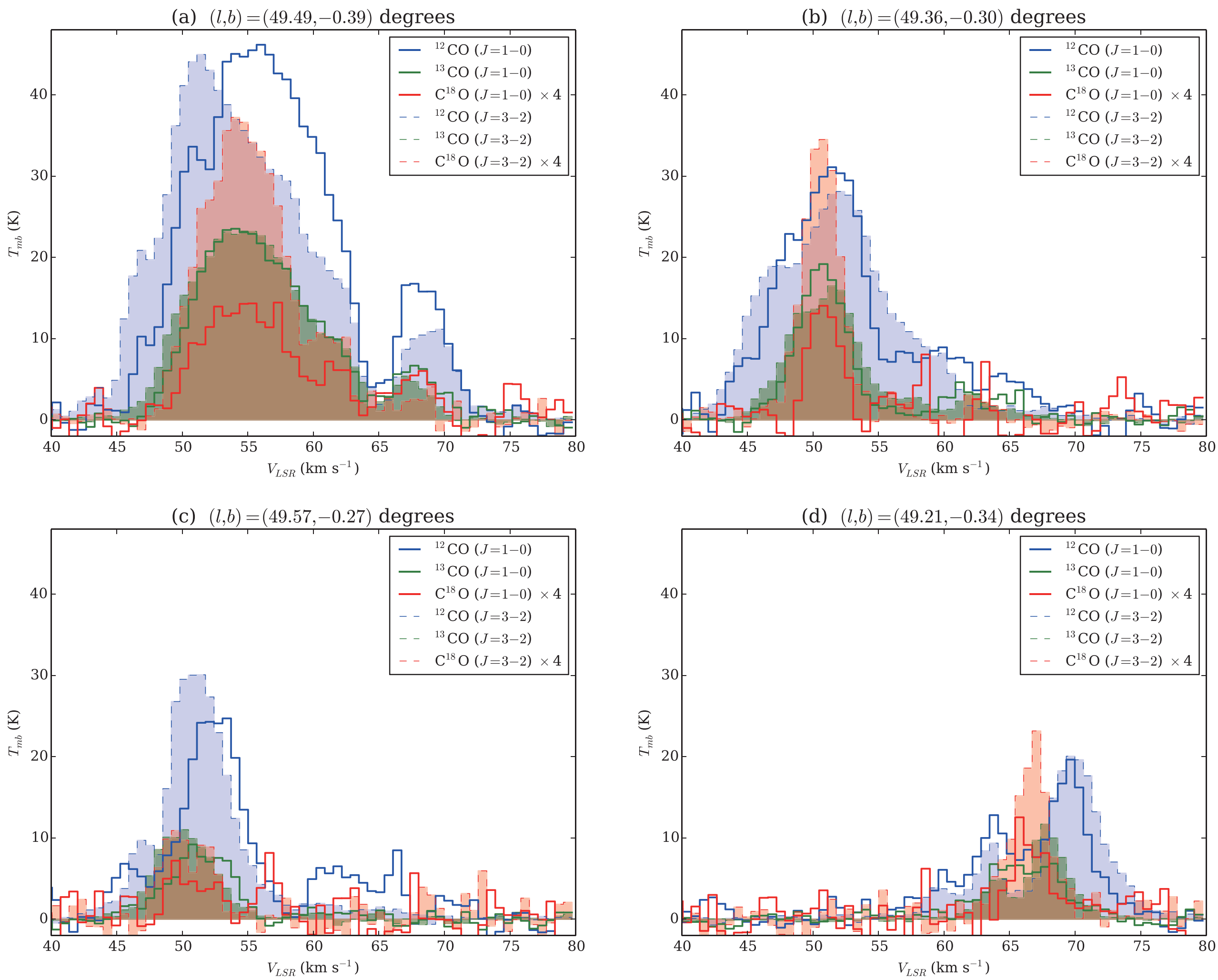

Fig. 3. The CO spectra at (a) $(l, b) = (49\overset{\circ}{.}49, -0\overset{\circ}{.}39)$, (b) $(l, b) = (49\overset{\circ}{.}36, -0\overset{\circ}{.}30)$, (c) $(l, b) = (49\overset{\circ}{.}57, 0\overset{\circ}{.}27)$, and (d) $(l, b) = (49\overset{\circ}{.}21, -0\overset{\circ}{.}34)$. The blue, green, and red lines indicate the profiles of the ^{12}CO, ^{13}CO, and C^{18}O emission lines, respectively. The intensities of the C^{18}O emission lines were multiplied by 4. The solid and broken lines (filled) indicate the profiles of the $J = 1$–0 and $J = 3$–2 emission lines, respectively. The spatial grid size and resolution are $8\overset{\prime\prime}{.}5$ ($= 0\overset{\circ}{.}0023$) and $\sim 30''$ ($= 0\overset{\circ}{.}0083$), respectively.

the velocity channel maps of the ^{12}CO, ^{13}CO, and C^{18}O emissions in figure 19, appendix 1, for additional information. The ^{12}CO emissions presented in figure 5 show extended gas distributions for the four clouds, while the ^{13}CO emissions show that the clouds have networks of clumpy and filamentary structures. C^{18}O probes only clumpy structures except for the 68 km s^{-1} cloud.

The 50 km s^{-1} cloud shown in panel (a) of figures 5–7 has strong intensity peaks toward G49.5−0.4 and G49.4−0.3. In the ^{13}CO emissions these peaks are connected with each other with filamentary structures roughly elongated along the northeast–southwest at $b \approx -0\overset{\circ}{.}38$–$-0\overset{\circ}{.}32$ (figure 6a), which are not apparent in the ^{12}CO emissions (figure 5a), whereas the C^{18}O emissions show fragmented distributions with sizes of ∼2–3 pc toward these peaks (figure 7a). We derived the total molecular mass of the 50 km s^{-1} cloud as $\sim 1.1 \times 10^5\, M_\odot$ using the ^{13}CO ($J = 1$–0) map in figure 6a with an assumption of local thermodynamic equilibrium (LTE; e.g., Kawamura et al. 1998). We adopted an abundance ratio [^{13}CO]/[H$_2$] of 1.5×10^{-6} (Dickman 1978), and we estimated an excitation temperature $T_{\rm ex}$ for each pixel from the value of the peak brightness temperature of the optically thick ^{12}CO ($J = 1$–0) emissions in the 50 km s^{-1} cloud.

The CO emissions in the 56 km s^{-1} cloud shown in panel (b) of figures 5–7 are enhanced at $(l, b) \approx (49\overset{\circ}{.}48, -0\overset{\circ}{.}40)$ in G49.5−0.4, whose CO intensities are strongest among the four velocity clouds in W 51 A. The ^{13}CO emissions show filamentary structures, and some of them are radially elongated from the CO peak at G49.5−0.4 (figure 6b), while the C^{18}O emission is detected only toward the peak with a size of ∼3 pc (figure 7b). The total molecular mass of the 56 km s^{-1} cloud measured using the ^{13}CO map in figure 6b is $\sim 1.3 \times 10^5\, M_\odot$.

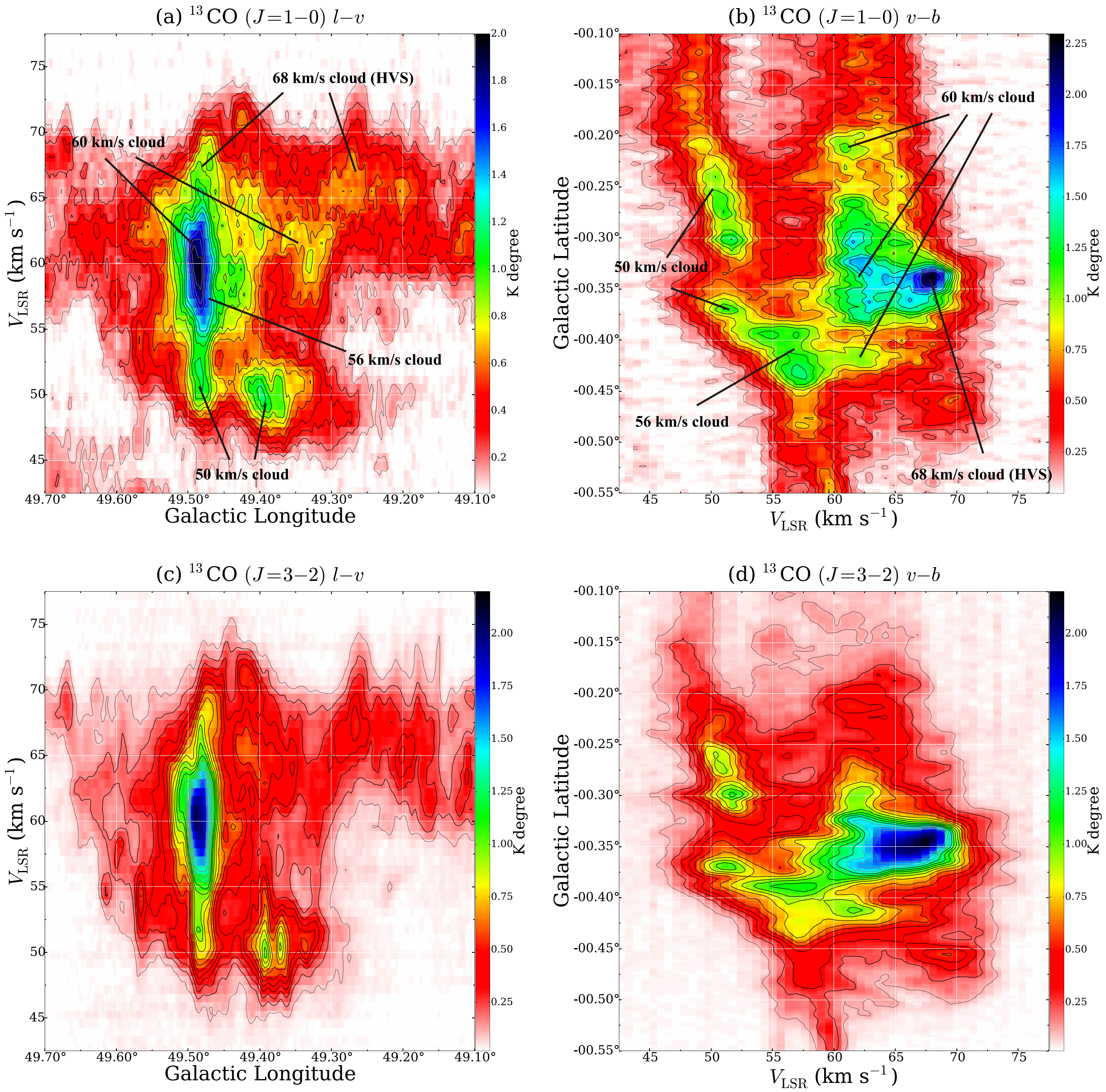

Fig. 4. (a) Galactic latitude–velocity (*l*–*v*) diagram of the ^{13}CO ($J = 1$–0) emissions integrated over $b = -0\overset{\circ}{.}55$–$-0\overset{\circ}{.}10$. The contours are plotted with 5σ (0.11 K deg) intervals starting from the 5σ (0.11 K deg) level. (b) Velocity–Galactic latitude (*v*–*b*) diagram of the ^{13}CO ($J = 1$–0) emissions integrated over $l = 49\overset{\circ}{.}70$–$49\overset{\circ}{.}10$. The contours are plotted with 5σ (0.13 K deg) intervals starting from the 5σ (0.13 K deg) level. (c) As panel (a), but for the ^{13}CO ($J = 3$–2) emissions. The contours are plotted at every 5σ (0.09 K deg) from 0.09 K deg ($\sim$5σ). (d) As panel (b), but for the ^{13}CO ($J = 3$–2) emissions. The contours are plotted with 5σ (0.11 K deg) intervals starting from the 5σ (0.11 K deg) level.

The 60 km s^{-1} cloud in panel (c) of figures 5–7 shows similar gas distribution to the 56 km s^{-1} cloud, as in the ^{13}CO emissions it consists of a strong CO peak at G49.5−0.4, attached with filamentary structures (figure 6c). A difference between the 50 and 56 km s^{-1} clouds is the diffuse ^{13}CO emissions extended above $b \approx -0\overset{\circ}{.}3$ between $l = 49\overset{\circ}{.}45$ and $49\overset{\circ}{.}30$. The total molecular mass of the 60 km s^{-1} cloud estimated with the ^{13}CO map is as large as $\sim 1.9 \times 10^5\,M_\odot$. The C^{18}O distribution in figure 7c is highly fragmented in G49.5−0.4 and G49.4−0.3. Note that the C^{18}O fragments distributed to the east of G49.4−0.3 at $(l, b) \approx (49\overset{\circ}{.}38, -0\overset{\circ}{.}32)$ correspond to part of the ^{13}CO filamentary structure which surrounds the 21 cm contours of G49.4−0.3 (figure 6c), suggesting possible interaction between the 60 km s^{-1} cloud and G49.4−0.3.

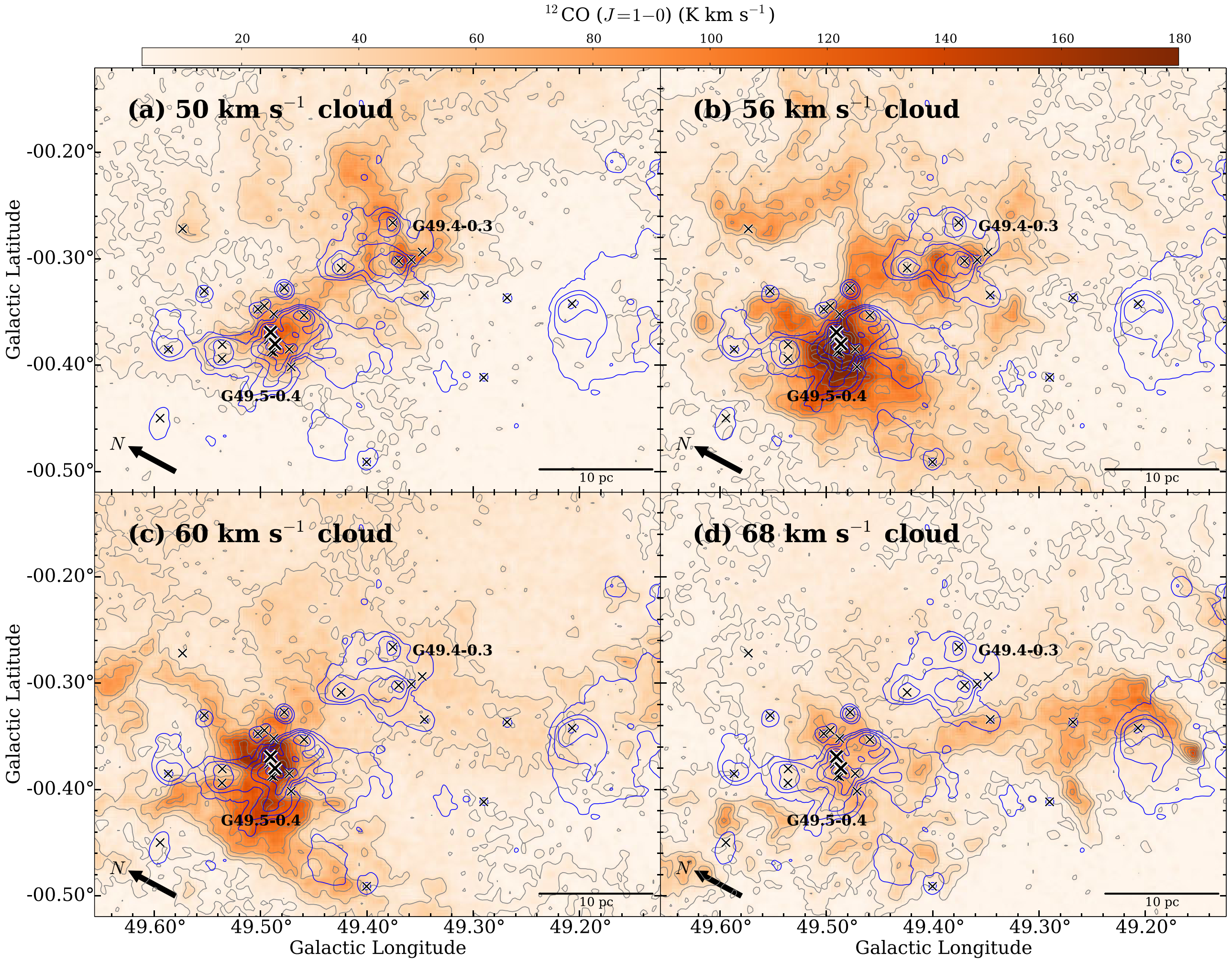

Fig. 5. The ^{12}CO (J = 1–0) integrated intensity distributions of the (a) 50, (b) 56, (c) 60, and (d). 68 km s^{-1} clouds, with integration ranges of 46.9–52.1, 52.8–58.6, 59.3–64.5, and 65.1–71.0 km s^{-1}, respectively. The gray contours are plotted with 6σ (20 K km s^{-1}) intervals starting from the 3σ (10 K km s^{-1}) level. The blue contours show the THOR 21 cm radio continuum emission combined with the VGPS data (Stil et al. 2006; Beuther et al. 2016), and are plotted from 0.06 to 3.0 Jy sr^{-1} in logarithmic steps. The angular resolution of the combined THOR and VGPS data is 25″. The crosses represent H II regions listed in Mehringer (1994).

In panel (d) of figures 5–7, the 68 km s^{-1} cloud has a filamentary structure elongated nearly parallel to the galactic plane between l = 49°.50 and 49°.20. The width of the filament can be measured as ∼4–8 pc in the ^{12}CO and ^{13}CO emissions, while it is thinner in the C^{18}O emissions, ∼3 pc. The northeastern tip of the filament is spatially coincident with G49.5−0.4, while the opposite end corresponds to the H II region G49.21−0.34. The total mass of the 68 km s^{-1} cloud is estimated as ∼1.3 × 10^5 $M_\odot$, which is consistent with the estimate in Carpenter and Sanders (1998).

3.1.2 CO (J = 3–2/J = 1–0) intensity ratios

Figures 8a–8d show large-scale distributions of the ^{13}CO (J = 3–2)/^{13}CO (J = 1–0) integrated intensity ratios (hereafter R^{13}_{3210}) of the four clouds in W 51 A (the associated errors of R^{13}_{3210} are presented in appendix 2). The four clouds typically have R^{13}_{3210} of higher than 0.6, up to over 2.0, while a low R^{13}_{3210} of less than 0.2 is seen in the diffuse gas widely distributed at b > −0°.30–−0°.20 and b < −0°.45. Moreover, to extract the molecular gas heated up by the massive stars in W 51 A, in figures 8e–8h we plot the ^{13}CO (J = 1–0) contour maps of the four clouds using only the voxels having R^{13}_{3210} higher than 1.0. In appendix 3 we perform large velocity gradient (LVG) analysis, indicating that an R^{13}_{3210} of higher than 1.0 can probe the high-temperature (>20 K) gas.

In G49.5−0.4, the high-R^{13}_{3210} gas is seen in all four clouds, and physical associations between these clouds and the H II regions in G49.5−0.4 are thus suggested. In G49.4−0.3, on the other hand, the filamentary structures seen in the 8 μm image are traced well by the high-R^{13}_{3210} gas

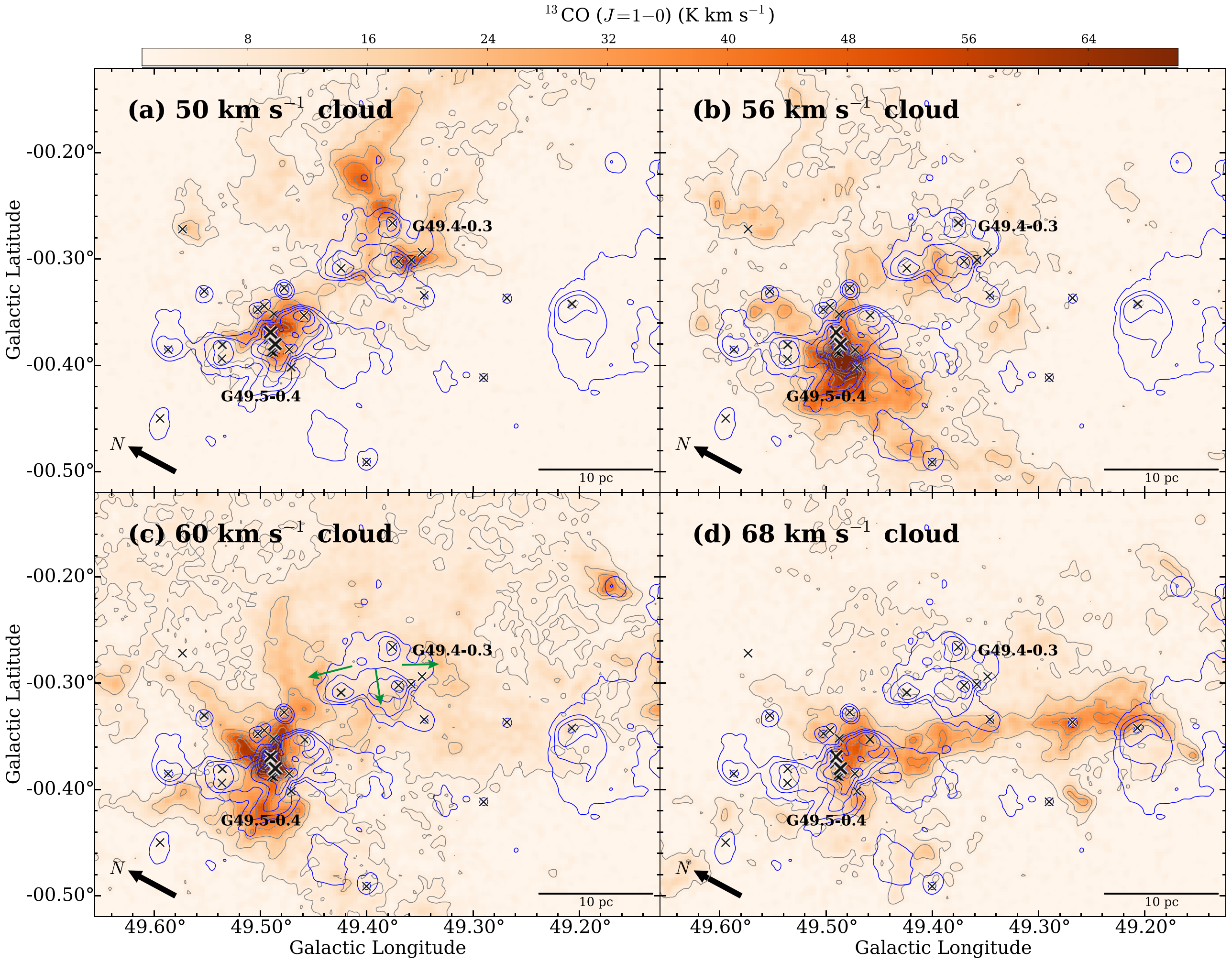

Fig. 6. As figure 5 but for the ^{13}CO (J = 1–0) emissions. The gray contours are plotted with 6σ (10 K km s^{-1}) intervals starting from the 3σ (5 K km s^{-1}) level.

in the 50 km s^{-1} cloud, forming an arch-like gas distribution (figures 8a and 8e). The 56 km s^{-1} cloud is also high in R^{13}_{3210} at the footpoints of the arch-like structure (figures 8b and 8f). In the 60 km s^{-1} cloud, high-R^{13}_{3210} gas surrounds the eastern and southeastern rim of the 21 cm emissions of G49.4−0.3 (figures 8c and 8g). The 68 km s^{-1} cloud shows a continuous distribution of high-R^{13}_{3210} gas between the east and the south of G49.4−0.3, although its association with G49.4−0.3 is not clear (figures 8d and 8h). These results indicate physical associations of multiple velocity components of gas between G49.5−0.4 and G49.4−0.3.

Associations of the other H II regions with the multiple velocity components can also be investigated in figures 8e–8h. G49.57−0.27 is an isolated H II region situated at the north of G49.5−0.4, and shows high R^{13}_{3210} in the 50 and 56 km s^{-1} clouds (figures 8e and 8f). There are several relatively expanded H II regions in G49.5−0.4, i.e., G49.5−0.4f, g, h, and i. Although we found no high-R^{13}_{3210} gas spatially overlapping these H II regions, there are several high-R^{13}_{3210} components in the 50, 56, and 60 km s^{-1} clouds which are distributed at the rims of the 21 cm continuum emissions of these H II regions (figures 8e–8g). As these four H II regions are relatively evolved, with ages of the order of 1 Myr as summarized in table 1, this high-R^{13}_{3210} gas can be interpreted as remnants of the natal molecular gas of the massive stars in these H II regions. In the other H II regions, we found no plausible signatures of physical association of multiple velocity components. These show either no high-R^{13}_{3210} gas in the four clouds (e.g., G49.29−0.41) or high-R^{13}_{3210} gas only in one cloud (e.g., G49.21−0.34, G49.27−0.34, and G49.59−0.45). In the next subsection we present the detailed gas distribution toward the individual H II regions which are likely associated with multiple velocity clouds.

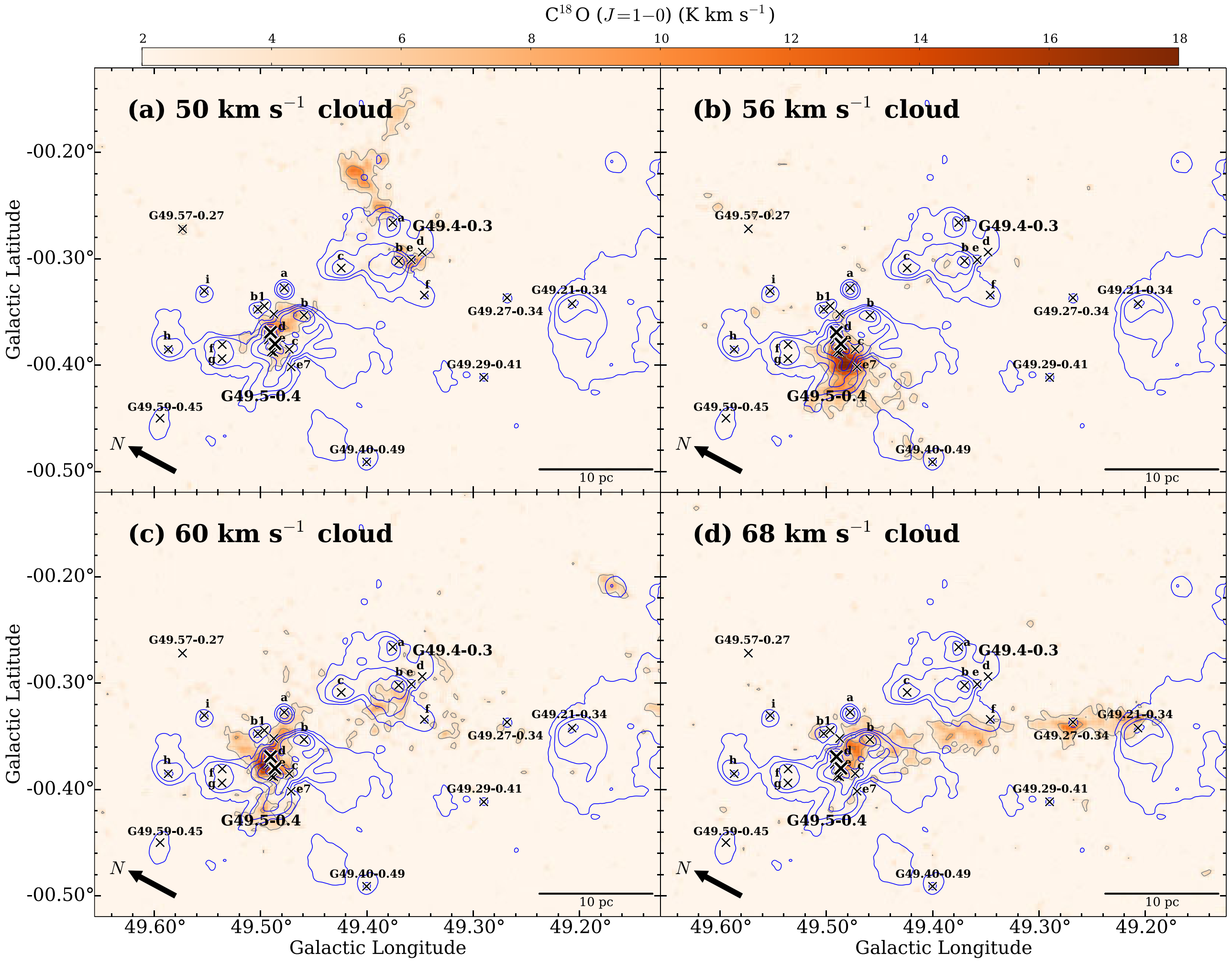

Fig. 7. As figure 5 but for the $C^{18}O$ ($J = 1$–0) emissions. The gray contours are plotted with 3σ (4 K km s^{-1}) intervals starting from the 3σ (4 K km s^{-1}) level.

3.2 Detailed gas distributions toward individual H II regions

3.2.1 G49.5−0.4

Figure 9 shows a close-up view of G49.5−0.4 with comparisons between the Spitzer 8 μm image (Carey et al. 2009) and the $C^{18}O$ contour maps of the four clouds, where the H II regions listed in table 1 are depicted by crosses, and the MYSOs identified by Saral et al. (2017) are plotted with triangles. The 8 μm emission is bright around $(l, b) \approx (49\overset{\circ}{.}45$–$49\overset{\circ}{.}49, -0\overset{\circ}{.}40$–$-0\overset{\circ}{.}33)$, at which many compact H II regions, including IRS 1 (G49.5−0.4e) and IRS 2 (G49.5−0.4d), are concentrated. Figure 9 shows that the four clouds have compact and bright $C^{18}O$ emissions within a few parsecs of the central 8 μm structure.

We identified $C^{18}O$ clumps in this region by drawing a contour at the 70% level of the maximum integrated intensity in the four clouds, resulting in discoveries of the four $C^{18}O$ clumps which are each embedded within the four clouds. Figure 10 shows the $C^{18}O$ ($J = 1$–0) spectra at the peak position of each clump. Velocities outside ± 5 km s^{-1} of each peak of the clump are plotted with dashed lines. The physical parameters are summarized in table 3. The FWHM velocity widths of each of the spectra are approximately 5–6 km s^{-1}. The peak column densities of the four clumps in the 50, 56, 60, and 68 km s^{-1} clouds are measured as 2.3, 4.4, 3.9, and 2.7 $\times$ 10^{23} cm^{-2}, respectively, from the $C^{18}O$ ($J = 1$–0) data by assuming LTE. We adopted here an abundance ratio of $[C^{18}O]/[H_2] = 1.7 \times 10^{-7}$ (Frerking et al. 1982). If we tentatively determine the radii of the clumps as 70% of the peak, the virial masses are estimated to be as in table 3, column (8). The LTE masses shown in table 3 column (5) are almost greater than the virial masses.

The color scale in figures 11a, 11b, and 11c show the $C^{18}O$ ($J = 1$–0) integrated intensity distributions of the 60 km s^{-1} cloud, and the blue contours show the $C^{18}O$ ($J =$ 1–0) integrated intensity distributions of (a) the 50 km s^{-1}

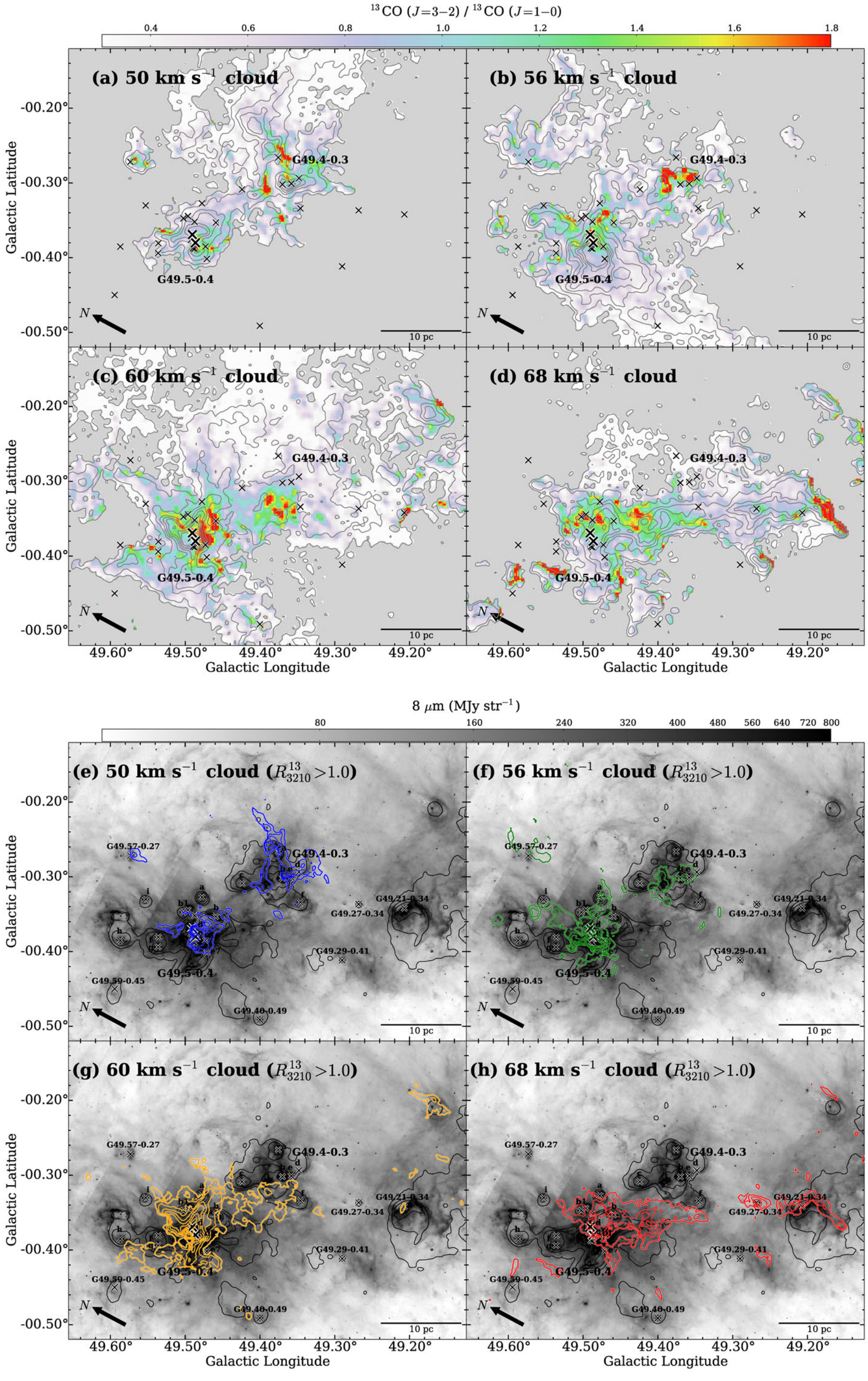

Fig. 8. (a)–(d) R^{13}_{3210} distributions of the four clouds. The contours indicate ^{13}CO ($J = 1$–0), and are plotted with $6\,\sigma$ ($10\,\mathrm{K\,km\,s^{-1}}$) intervals starting from the $6\,\sigma$ ($10\,\mathrm{K\,km\,s^{-1}}$) level for panels (a)–(c), and $6\,\sigma$ ($5\,\mathrm{K\,km\,s^{-1}}$) intervals starting from the $5\,\sigma$ ($8\,\mathrm{K\,km\,s^{-1}}$) level for panel (d). The associated errors of R^{13}_{3210} for each pixel are presented in figure 20 in appendix 2. (e)–(h) The spatial distributions of the high-R^{13}_{3210} gas are shown in the colored contour maps, where the high-R^{13}_{3210} data was made by integrating only the voxels having $R^{13}_{3210} > 1.0$. The colored contours are plotted at the same levels as in panels (a)–(d). The background image is the Spitzer $8\,\mu$m image, while the black contours represent the 21 cm continuum emissions plotted at the same levels as those in figure 5. The crosses are the same as those in figure 5.

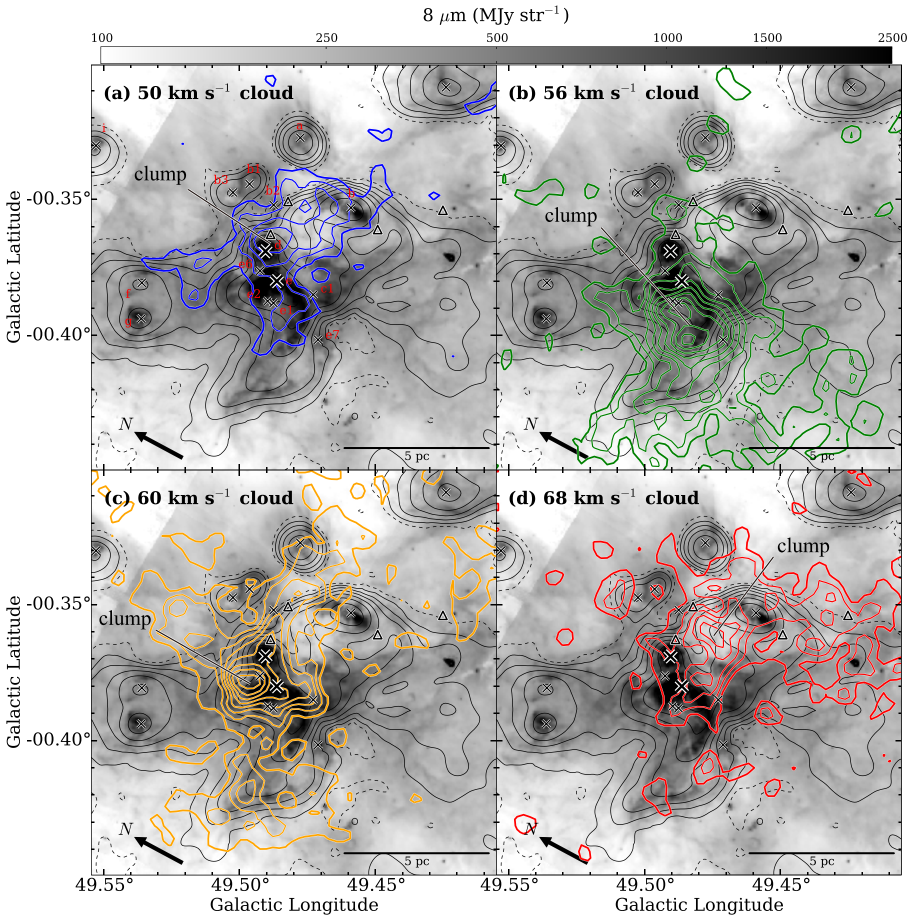

Fig. 9. C^{18}O ($J = 1$–0) integrated intensity distributions of the four velocity clouds in G49.5−0.4 are presented as colored contour maps superimposed on the Spitzer 8 μm image (Carey et al. 2009). The colored contours are plotted with 2 K km s^{-1} intervals starting from the 3 K km s^{-1} level, where the rms noise level of the image is ∼1.5 K km s^{-1}. The H II regions listed in table 1 are depicted by crosses, and the massive young stars identified by Saral et al. (2017) are plotted with triangles. The black contours show the 21 cm continuum emissions plotted from 0.03 (dashed lines) to 3.0 Jy sr^{-1} in logarithmic steps.

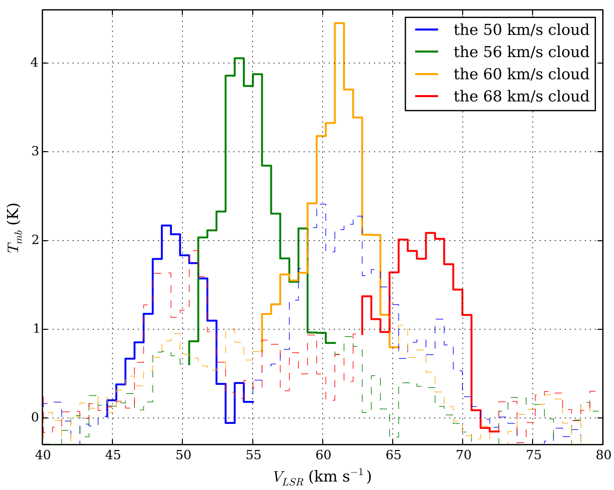

Fig. 10. The C^{18}O ($J = 1$–0) spectra at the peak position (see table 3) of each clump embedded in the 50 km s^{-1} (blue), 56 km s^{-1} (green), 60 km s^{-1} (orange), and 68 km s^{-1} (red) cloud. Velocities outside ±5 km s^{-1} of each peak of the clump are plotted with dashed lines.

cloud, (b) the 56 km s^{-1} cloud, and (c) the 68 km s^{-1} cloud, respectively. In figure 11a, the 60 km s^{-1} cloud surrounds the peak of the 50 km s^{-1} cloud. In figure 11b, the 56 km s^{-1} cloud and the 60 km s^{-1} cloud show a complementary distribution. Futhermore, in figure 11c, the 60 km s^{-1} cloud and the 68 km s^{-1} cloud also show a complementary distribution. The complementary distribution between the 60 and 68 km s^{-1} clouds was discussed by Carpenter and Sanders (1998) based on their CO observations, and a CCC scenario between these two clouds were suggested by the authors.

Figure 12a shows comparisons of the identified four C^{18}O clumps superimposed on the Spitzer 8 μm image, where the C^{18}O ($J = 1$–0) contours are plotted at 60%, 70%, 80%, and 90% of the peak intensities of the clumps. Although these four clumps are concentrated within a small area of less than 5 pc, they are not spatially coincident along the line of sight, showing a complementary distribution. Our CO data newly revealed that the complementary

Table 3. Parameters of the $C^{18}O$ (J = 1–0) clumps in G49.5−0.4 and G49.4−0.3.*

Cloud name (1)	Peak position (l, b) (2)	$C^{18}O$ (1–0) W_{max} (K km s^{-1}) (3)	R (70%) (pc) (4)	M_{LTE} (70%) (10^4 $M_\odot$) (5)	$N_{max}(H_2)$ (10^{23} cm^{-2}) (6)	FWHM (km s^{-1}) (7)	M_{vir} (10^4 $M_\odot$) (8)
G49.5−0.4							
50 km s^{-1} cloud	49°.492, −0°.365	11.0	∼1.1	0.9 ± 0.1	2.3 ± 0.2	4.7 ± 0.2	0.6 ± 0.1
56 km s^{-1} cloud	49°.485, −0°.400	19.7	∼1.1	2.3 ± 0.1	4.4 ± 0.4	6.3 ± 0.5	1.0 ± 0.2
60 km s^{-1} cloud	49°.495, −0°.379	18.0	∼0.8	1.0 ± 0.1	3.9 ± 0.4	6.0 ± 0.5	0.7 ± 0.1
68 km s^{-1} cloud	49°.473, −0°.360	12.2	∼1.0	1.4 ± 0.1	2.7 ± 0.3	6.4 ± 0.7	1.0 ± 0.2
G49.4−0.3							
50 km s^{-1} cloud	49°.360, −0°.303	13.3	∼0.8	0.3 ± 0.1	2.1 ± 0.2	3.2 ± 0.1	0.2 ± 0.1
56 km s^{-1} cloud	—	—	—	—	—	—	—
60 km s^{-1} cloud	49°.391, −0°.322	8.5	∼0.9	0.4 ± 0.1	1.8 ± 0.2	4.2 ± 0.5	0.4 ± 0.1
68 km s^{-1} cloud	49°.355, −0°.355	10.2	∼2.5 ×1.0	1.6 ± 0.2	2.1 ± 0.2	4.2 ± 0.3	0.7 ± 0.1

* (1) Name of the cloud in which the clump is embedded. (2) Peak position of the $C^{18}O$ (J = 1–0) integrated intensity. (3) Peak integrated intensity the $C^{18}O$ (J = 1–0). (4) Effective radius of the clump, which was measured at 70% of the peak intensity of the clump. (5) Molecular mass derived from $C^{18}O$ (J = 1–0) intensity maps assuming LTE within the 70% radius. (6) Maximum H_2 column density of the clump. (7) FWHM of the $C^{18}O$ (J = 1–0) spectrum at the peak position. These are derived by Gaussian fitting. (8) Virial mass derived from columns (4) and (7): $R\Delta v^2/G$, where Δv and G are the FWHM and the gravitational constant, respectively.

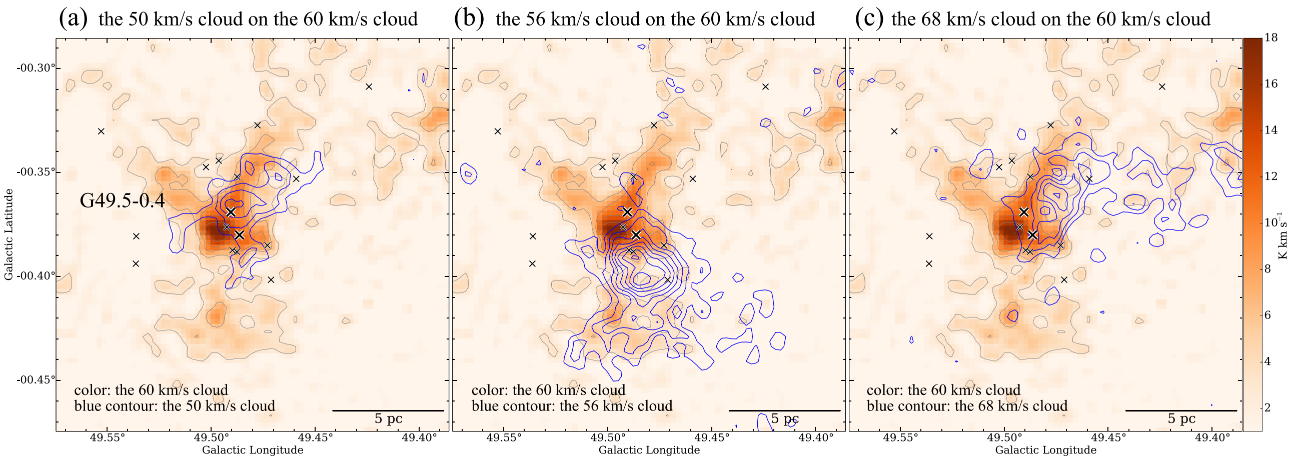

Fig. 11. (a) $C^{18}O$ (J = 1–0) integrated intensity distributions of the 60 km s^{-1} cloud. The blue contours show the $C^{18}O$ (J = 1–0) integrated intensity distributions of the 50 km s^{-1} cloud, and are plotted with 1.5σ (2 K km s^{-1}) intervals starting from the 3σ (4 K km s^{-1}) level. The H II regions listed in table 1 are denoted by crosses. (b) As (a), but the blue contours show the $C^{18}O$ (J = 1–0) integrated intensity distributions of the 56 km s^{-1} cloud. (c) As (a), but the blue contours show the $C^{18}O$ (J = 1–0) integrated intensity distributions of the 68 km s^{-1} cloud.

distribution is seen not only for the 60 and 68 km s^{-1} clouds, but also for all four clouds.

The compact H II regions depicted by crosses are distributed around the rims of these four clumps. IRS 2 (G49.5−0.4d) is distributed at the interface of the clumps between the 50 and 60 km s^{-1} clouds, while IRS 1 (G49.5−0.4e) is seen at the boundaries of the 56, 60, and 68 km s^{-1} clouds. The other H II regions, G49.5−0.4e1, e2, and e6, are also distributed at the interface of the four clouds, where the 8 μm emission is also enhanced (figure 12a). The v–b diagram of the ^{13}CO and $C^{18}O$ (J = 1–0) emissions shown in figure 12b indicates that the four clumps are connected with each other by the CO emissions with intermediate intensities. These intermediate velocity features are possibly interpreted as the broad bridge features created in the CCC process as discussed in subsection 1.2.

Figure 12c shows the v–b diagram for R^{13}_{3210}. High R^{13}_{3210} (>1.5) is seen at the velocity edge and the intermediate velocity of the clouds. In the central molecular zone of the Galaxy, a spectacular star-forming environment, Oka et al. (2007) also reported a high CO J = 3–2/J = 1–0 ratio of >1.5. The high R^{13}_{3210} in G49.5−0.4 is probably caused by feedback from the massive stars and/or collisional heating between the clouds.

3.2.2 G49.4−0.3

Figure 13 shows the ^{13}CO (J = 1–0) contour maps of the four clouds toward G49.4−0.3. The velocity ranges

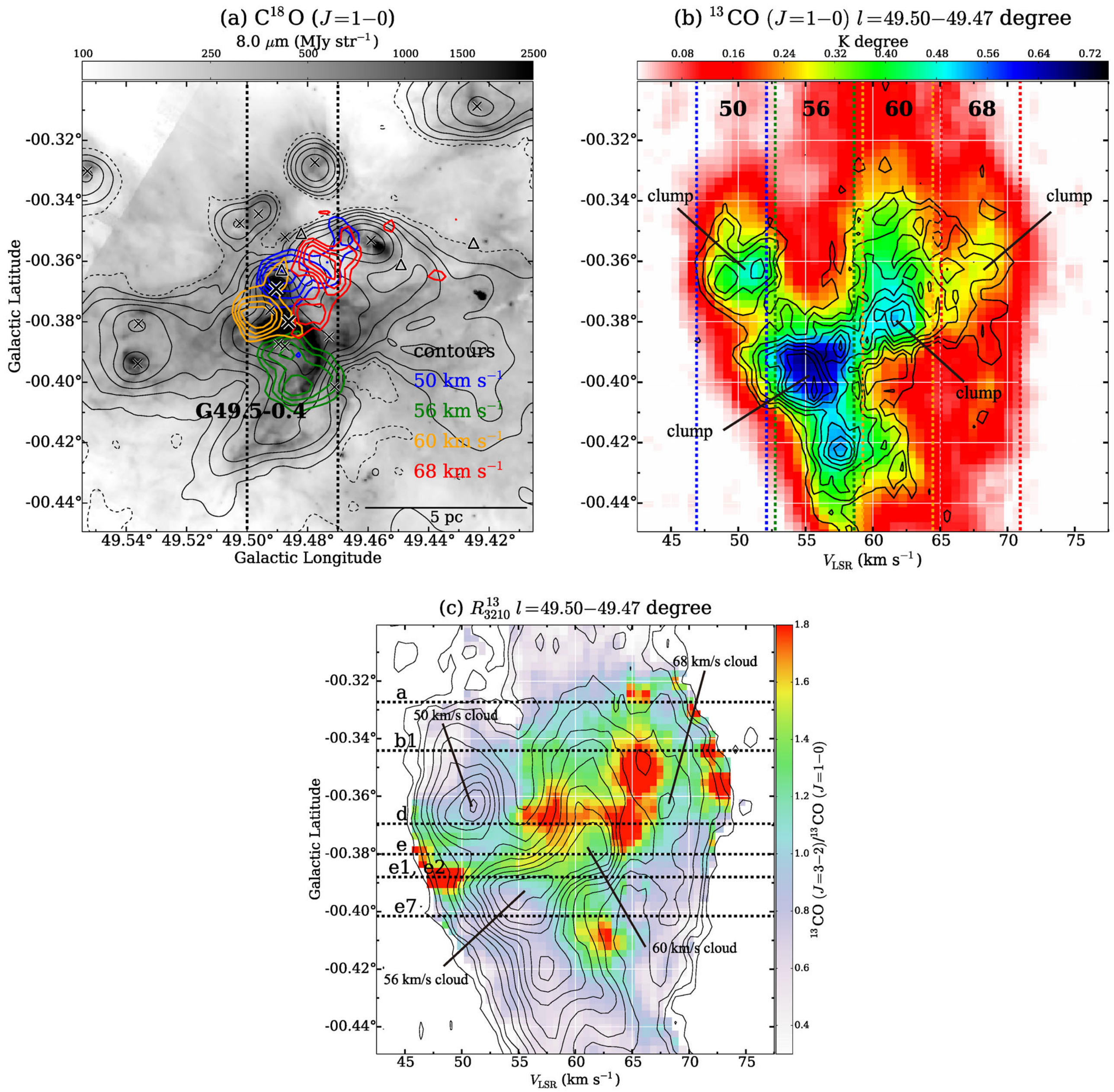

Fig. 12. (a) The contour maps of the $C^{18}O$ ($J = 1$–0) emissions of the four clouds around G49.5−0.4 are plotted superimposed on the Spitzer 8 μm image and 21 cm contour map. The $C^{18}O$ ($J = 1$–0) contours are plotted at 60%, 70%, 80%, and 90% of the peak intensities of the four clumps. The black contours show the 21 cm continuum emissions plotted from 0.03 (dashed lines) to 3.0 Jy sr^{-1} with logarithmic steps. (b) Velocity–Galactic latitude (v–b) diagram of the ^{13}CO ($J = 1$–0) emissions (color) and $C^{18}O$ ($J = 1$–0) emissions (contours) toward G49.5−0.4 integrated over l = 49.°50–49.°47, where the contours are plotted with 5σ (0.03 K deg) intervals starting from the 5σ (0.03 K deg) level. The vertical dashed lines show the integration ranges of the four clouds presented in figures 9 and 12a. (c) The v–b diagram of the R^{13}_{3210} distributions toward G49.5−0.4 integrated over l = 49.°50–49.°47. The contours show the intensity of the ^{13}CO ($J = 1$–0) emissions. The horizontal dashed lines indicate the position of the compact H II regions G49.5−0.4a, b, d, e, e1, e2, and e7.

of the four clouds in each panel are determined from the v–b diagram plotted in figure 14b. As already presented in figure 8, the arch-like CO structure in the 50 km s^{-1} cloud in figure 13a is spatially correlated with the bright 8 μm emissions, which consist of a network of filamentary structures elongated nearly parallel or perpendicular to the Galactic plane. The 8 μm filaments include the H II regions G49.4−0.3a, b, c, d, and e (see table 1) and MYSOs. Of these, G49.4−0.3a, b, and e are spatially coincident with the 50 km s^{-1} cloud, as discussed by Kang et al. (2010).

The 56 km s^{-1} cloud in figure 13b shows diffuse ^{13}CO emissions around the footpoints of the arch-like structure. In addition, there are three CO components, which appear to surround the 21 cm counters of G49.4−0.3, at

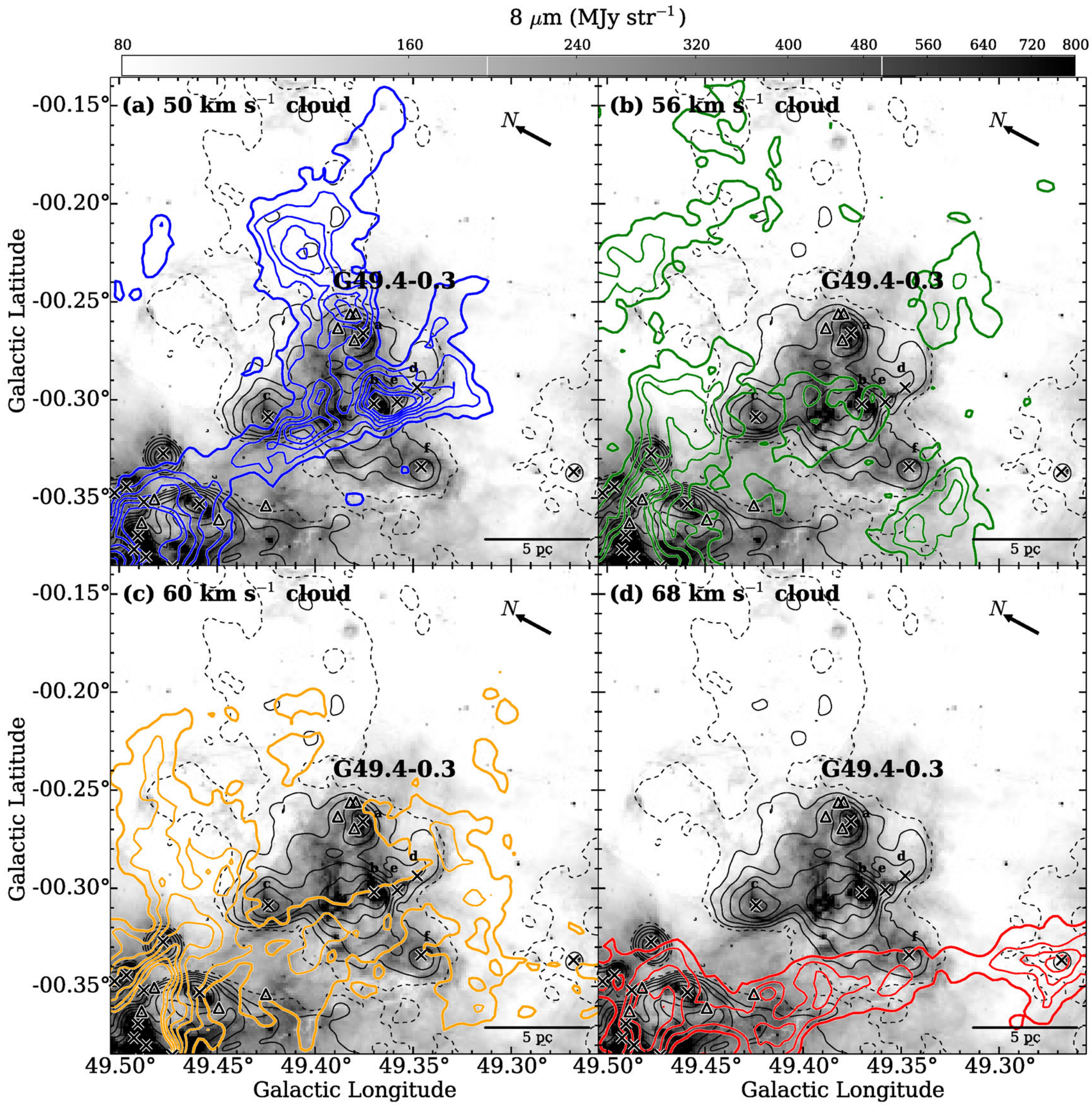

Fig. 13. ^{13}CO ($J = 1$–0) integrated intensity distributions of the four velocity clouds in G49.4−0.3 are presented as colored contour maps superimposed on the Spitzer 8 μm image (Carey et al. 2009). The velocity ranges of the ^{13}CO emissions in panels (a)–(d) are 46.9–55.4, 55.4–59.3, 59.3–64.5, and 64.5–71.0 km s^{-1}, and the contours are plotted with 8 K km s^{-1} intervals starting from the 18 K km s^{-1} level for panel (a), 4 K km s^{-1} intervals starting from the 4 K km s^{-1} level for panel (b), 6 K km s^{-1} intervals starting from the 12 K km s^{-1} level for panel (c), and 8 K km s^{-1} intervals starting from the 12 K km s^{-1} level for panel (d), respectively, where the rms noise level of the images is ~1.5 K km s^{-1}. The black contours show the 21 cm emissions plotted at the same levels as those in figure 5. The H II regions listed in table 1 are depicted by crosses, and the MYSOs identified by Saral et al. (2017) are plotted with triangles.

(l, b) ≈ (49°.32, −0°.25), (49°.33, −0°.36), and (40°.46, −0°.31). In figure 13c the filamentary structures of the 60 km s^{-1} cloud shown in figure 6c are plotted. The 8 μm filaments stretched nearly parallel to the Galactic plane are traced by the upper rim of the ^{13}CO filamentary structure of the 60 km s^{-1} cloud at $l \approx$ 49°.34–49°.43 and $b \approx$ −0°.32–−0°.30. The ^{13}CO filamentary structure harbors high-R^{13}_{3210} gas at the same l range, as shown in figure 8. The 68 km s^{-1} cloud (HVS) in figure 13d is distributed almost parallel to the filamentary structure in the 60 km s^{-1} cloud.

Figure 14a presents the C^{18}O distributions of the four clouds toward G49.4−0.3 in the same manner as in figure 12a. While the 56 km s^{-1} cloud is not detected in C^{18}O, the 60 and 68 km s^{-1} clouds show fragmented distribution at $l \approx$ 49°.34–49°.40, and are aligned along the Galactic latitude with the 50 km s^{-1} cloud, showing a complementary distribution. The v–b diagram for this l range is presented in figure 14b, which shows that the 60 and 68 km s^{-1} clouds are bridged by the C^{18}O emissions at the intermediate velocities, while the 50 and 60 km s^{-1} clouds are connected with the ^{12}CO emissions at $b \approx$ −0°.32–−0°.29 for 55–60 km s^{-1}, where the spatial distribution of the latter connecting feature is shown in figure 13b in ^{13}CO. These intermediate velocity features may be

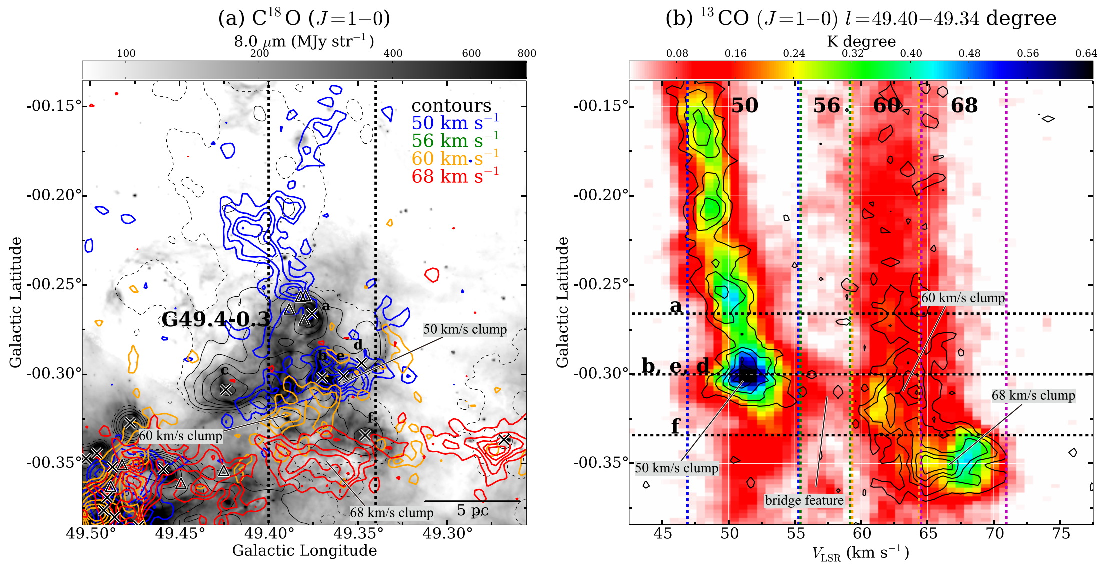

Fig. 14. (a) Colored contour maps (blue, green, orange, and red) of the $C^{18}O$ emissions of the four clouds around G49.4−0.3 are plotted superimposed on the Spitzer 8 μm image and 21 cm contour map (black). The $C^{18}O$ contours are plotted with 2 K km s^{-1} intervals starting from the 3σ (4 K km s^{-1}) level. The crosses represent compact H II regions listed by Mehringer (1994)—see table 1—while the MYSOs identified by Saral et al. (2017) are plotted with triangles. (b) Velocity–Galactic latitude (v–b) diagram of ^{13}CO (J = 1–0) integrated over l = 49°.40–49°.34. The contours indicate the $C^{18}O$ (J = 1–0) emissions and are plotted with 3σ (0.02 K deg) intervals starting from the 3σ (0.02 K deg) level. Horizontal dashed lines indicate the positions of compact H II regions, while the vertical dashed lines show the integration ranges of the four clouds presented in figures 13 and 14a.

interpreted as the broad bridge features that suggest interactions between different velocity components. Compared to the 8 μm emissions in figure 14a, the $C^{18}O$ emissions of the 60 and 68 km s^{-1} clouds correspond to the regions where the 8 μm emission is faint. The column density $N(H_2)$ of the 60 km s^{-1} and 68 km s^{-1} clouds are typically 0.6–1.0 × 10^{23} cm^{-2} (the column density maps are presented in appendix 4), which corresponds to $A_V \approx$ 32–53 mag (Shetty et al. 2011). Cardelli, Clayton, and Mathis (1989) and Indebetouw et al. (2005) reported $A_V/A_K \approx 8.8$ ($R_V \approx 3.1$) and $A_{[8.0\,\mu m]}/A_K \approx 0.43$, respectively. Therefore, $N(H_2)$ of 0.6–1.0 × 10^{23} cm^{-2} corresponds $A_{[8.0\,\mu m]} \approx$ 1.5–2.6 mag. The faintness of the 8 μm emission is considered to be extinction by the 60 km s^{-1} and 68 km s^{-1} clouds, suggesting that these two clouds are both located in front of the nebulosities of G49.4−0.3 (Ginsburg et al. 2015), lending further support to the idea that these two clouds are distributed at the same location. At the top of the arch-like structure of the 50 km s^{-1} cloud, where G49.4−0.3a and several MYSOs are distributed, we cannot find complementary distribution among different velocity components, while there is possibly a bridge feature in the ^{13}CO emissions between the 50 and 60 km s^{-1} clouds at $b \approx -0°.24$ (figure 14b).

3.2.3 G49.57−0.27

As presented in figure 8, G49.57−0.27 shows high R^{13}_{3210} in the 50 and 56 km s^{-1} clouds. G49.57−0.27 is an isolated compact H II region located at (l, b) ≈ (49°.57, −0°.27), whose ionizing photon flux measured from a 21 cm continuum map corresponds to a spectral type of B0 (see table 1). Figure 15a shows the ^{13}CO (J = 1–0) integrated intensity maps of the 50 and 56 km s^{-1} clouds in contours and color, respectively. The CO emission in the 50 km s^{-1} cloud shows a roughly circular distribution with a diameter of ∼3 pc, and is spatially coincident with G49.57−0.27 depicted by a cross in figure 15a. On the other hand, the 56 km s^{-1} cloud shows two components separated along the Galactic longitude, and the 50 km s^{-1} component is sandwiched by these two components, indicating a complementary distribution. In the l–v diagram in figure 15b, the 50 km s^{-1} component is connected with the two separated components in the 56 km s^{-1} cloud, showing a "V-shaped" gas distribution in the ^{12}CO (J = 1–0) emissions. As introduced in section 2, detections of V-shaped gas distribution in the p–v diagram were reported in several CCC regions (e.g., Fukui et al. 2018a; Ohama et al. 2018b; Hayashi et al. 2018; Torii et al. 2021). Based on the synthetic CO observations performed by Haworth et al. (2015b) using the CCC scenarios of Takahira, Tasker, and Habe (2014), Fukui et al. (2018a) and Torii et al. (2021) reproduced the V-shaped gas distribution in the p–v diagram (see figure 14 of Fukui et al. 2018a), which resembles the present CO observations shown in figure 15a.

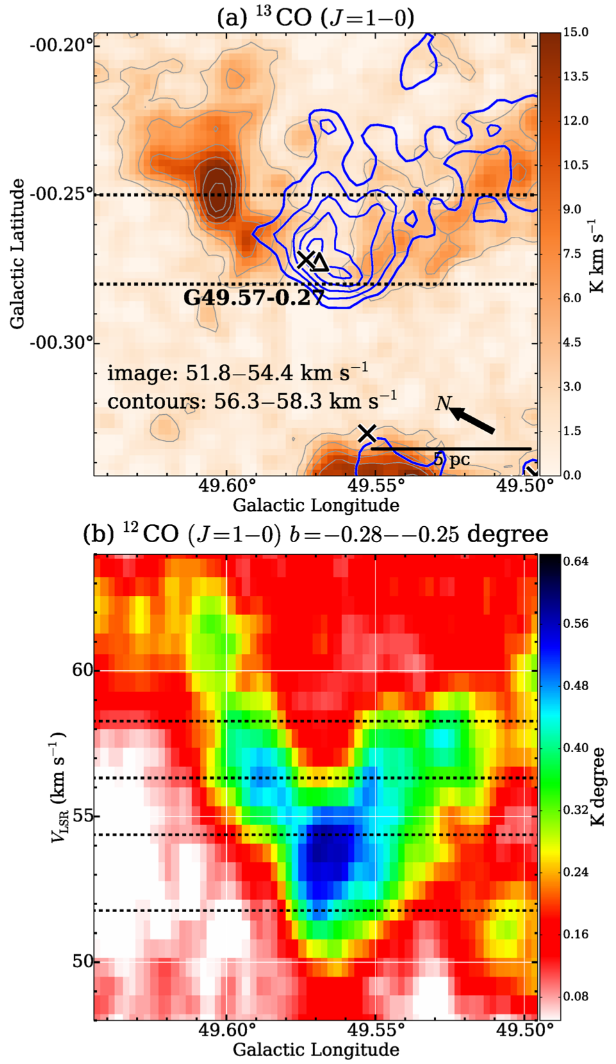

Fig. 15. (a) Complementary distributions of the two velocity components toward G49.57−0.27. The color scale shows ^{13}CO (J = 1–0) for 56.3–58.3 km s^{-1}, while the blue contours show ^{13}CO (J = 1–0) for 51.8–54.4 km s^{-1}. The blue contours are plotted with 3σ (4 K km s^{-1}) intervals starting from the 5σ (6 K km s^{-1}) level. The crosses represent compact H II regions listed by Mehringer (1994)—table 1—while the MYSOs identified by Saral et al. (2017) are plotted with triangles. (b) Galactic longitude–velocity diagram of the ^{12}CO (J = 1–0) emission toward G49.57−0.27. The integration range in b is shown in panel (a) with vertical dashed lines.

4 Discussion

Our analyses of the new CO (J = 1–0) data have basically confirmed the observed features in the previous studies of Carpenter and Sanders (1998) and Okumura et al. (2001). In addition, our CO data, including the C^{18}O (J = 1–0) emission, revealed previously unreported signatures that can be summarized as follows:

(1) At the center of G49.5−0.4, in which IRS 1 and IRS 2 are located, the four C^{18}O clumps, which are each embedded within the four velocity clouds, show a complementary distribution within a small area of less than 5 pc (figure 11). These are connected with each other in the p–v diagram with ^{13}CO and/or C^{18}O emissions (figure 12), suggesting broad bridge features.

(2) In G49.4−0.3, the ^{13}CO filamentary structures in the 50, 60, and 68 km s^{-1} clouds elongated nearly parallel to the Galactic plane are aligned (figure 6). These filamentary structures show high R^{13}_{3210} near G49.4−0.3 (figure 8), suggesting physical associations with G49.4−0.3. Each pair of the 50 and 60 km s^{-1} clouds and the 60 and 68 km s^{-1} clouds are connected with the bridge features in the p–v diagram (figure 14).

(3) In the relatively evolved H II regions with larger sizes, i.e., G49.5−0.4f, g, h, and i, we found no CO counterparts spatially coincident with the H II regions along the line of sight, but identified remnant CO fragments in the 50, 56, and 60 km s^{-1} clouds (e.g., figure 6), which have high R^{13}_{3210} at the rims of these H II regions (figure 8).

(4) In the isolated H II region G49.57−0.27, a complementary distribution between the gas components in the 50 and 56 km s^{-1} clouds were discovered (figure 15), where the circular CO emission in the 50 km s^{-1} cloud is sandwiched by the two separated components in the 56 km s^{-1} cloud. The complementary distribution is seen as a V-shaped gas distribution in the l–v diagram, which is reproduced well by numerical calculations of CCC.

In this section we discuss a CCC scenario in W 51 A based on the results summarized above.

4.1 Ages of the H II regions

It is important to obtain the ages of the H II regions in W 51 A in order to discuss the formation mechanism of their exciting stars. Okumura et al. (2000) estimated the ages of several of the H II regions listed in table 1 by measuring the sizes of the H II regions. We calculated the ages of the remaining H II regions using the analytical model of D-type expansion developed by Spitzer (1978), where the sizes of the H II regions and classifications of the exciting sources summarized in table 1 were adopted. This calculation method is the same as the method used by Okumura et al. (2000). We assumed a uniform initial density of gas of 10^4 cm^{-3}, as the dense gas probed using C^{18}O is widely detected in the molecular clouds in W 51 A. The electron temperature was also assumed to be a constant value, 8000 K (e.g., Spitzer 1978). The ages estimated in this study are marked in table 1. G49.5−0.4 includes H II regions with various ages (0.1–2.6 Myr), while G49.4−0.3 includes only H II regions with ages of <1 Myr.

4.2 CCC scenarios in W 51 A

There are two main CCC scenarios in W 51 A discussed by the previous studies of Carpenter and Sanders (1998) and Okumura et al. (2001). Carpenter and Sanders (1998) assumed that the present 50, 56, and 60 km s^{-1} clouds, which correspond to the 53, 58, 60, and 63 km s^{-1} components in Carpenter and Sanders (1998), are inner clouds of a single GMC (the W 51 GMC). The authors discovered that the northern tip of the 68 km s^{-1} cloud is truncated at the location of the 60 km s^{-1} clouds. Although no detailed process was discussed to create such a complementary distribution, Carpenter and Sanders (1998) postulated a CCC scenario between the W 51 GMC and the 68 km s^{-1} cloud.

On the other hand, based on the ^{13}CO ($J = 1$–0) observations in G49.5−0.4, Okumura et al. (2001) discussed CCCs for two pairs of the clouds, i.e., the 56 and 60 km s^{-1} clouds and the 60 and 68 km s^{-1} clouds. Although the authors found no plausible evidence of collision between the 50 and 56 km s^{-1} clouds, they postulated a CCC scenario that four discrete molecular clouds distributed in a line along the line of sight are moving at different velocities, resulting in a "pileup" of these four clouds.

Our results provide new insight into the CCCs in the W 51 A region. Figures 11 and 12a indicate that the 50, 56, 60, and 68 km s^{-1} clouds show a complementary distribution. As introduced in subsection 1.2, the recent works on CCC indicate that a complementary distribution can be created through a collision of two molecular clouds of different sizes or with a spatial offset (Torii et al. 2011; Fukui et al. 2018a). If so, the present results suggest that multiple collisions of the four clouds have perhaps occurred in G49.5−0.4, resulting in the formation of the massive stars at the interfaces of the collisions. In this scenario, it is reasonably assumed that the observed C^{18}O clumps were formed through strong compression by the collisions. That the several compact H II regions are concentrated around the interfaces of the complementary distribution lends more credence to this CCC scenario. In figure 11a we could not observe a clear complementary distribution as in figures 11b and 11c.

In G49.5−0.4, the total mass of the dense gas is estimated to be $\sim 5 \times 10^4\,M_\odot$, and ∼30 O-stars have been identified (Okumura et al. 2000). If we assume that (1) one O-star was formed in one massive core, and (2) the mass of each massive core is 100 $M_\odot$, which is a value used as an initial mass of the massive core in the simulation of the massive star formation performed by Krumholz et al. (2009), the massive core formation efficiency in the dense gas is estimated to be ∼6%. This estimation is coarse. To estimate with high accuracy, observational studies with higher spatial resolution are required.

The timescale of the collisions in G49.5−0.4 can be approximately estimated from the ratio of the cloud size and the relative velocity between the two clouds. If we assume sizes of the four clumps of ∼2 pc (table 3) and relative velocities of 4–18 km s^{-1}, the estimated timescales of the collisions in G49.5−0.4 lie in the range 0.1–0.5 Myr. These figures are consistent with the estimated ages of the H II regions distributed around the interfaces of the complementary distribution, which include IRS 1 and IRS 2 (table 1). While our results indicate that the 50, 56, and 60 km s^{-1} clouds are almost blended within a small volume, which is consistent with the discussion by Ginsburg et al. (2015) based on the H_2CO absorption observations, the spatial correlation of the 68 km s^{-1} cloud with the extinction in the 8 μm emission (see figure 9d) shows that it is located in front of G49.5−0.4, not blended with the other three clouds.

In G49.4−0.3, the complementary distribution of gas and the presence of the bridge features suggest collisions of the 50 and 60 km s^{-1} clouds and the 60 and 68 km s^{-1} clouds (figure 14). As the filamentary structures in the 60 km s^{-1} cloud appear to surround the 21 cm continuum emissions of G49.4−0.3 (figure 6c), it is also possible to interpret the associations of the multiple velocity components in G49.4−0.3 as being expansion of the H II regions. If so, as the 60 km s^{-1} cloud is redshifted relative to the systemic velocity of the H II regions in G49.4−0.3, having velocities of ∼52 km s^{-1} (Ginsburg et al. 2015), it should be located behind G49.4−0.3. However, as seen in figure 14a, the C^{18}O components in the 60 km s^{-1} cloud coincide with the extinction in the 8 μm image. This indicates that it is located in front of G49.4−0.3 (Ginsburg et al. 2015), against the assumption of expansion of the H II region. On the other hand, in the CCC scenario the bridge feature in the p–v diagram indicates that the collision is ongoing, and it is possible that the 60 km s^{-1} cloud has not completely passed over G49.4−0.3 along the line of sight yet. In the CCC scenario, the dissipative effect of the H II regions can still work on the 60 km s^{-1} cloud to form CO components which surround G49.4−0.3 (indicated by green arrows in figure 6c), suggesting that the 60 km s^{-1} cloud originally had an extended gas distribution in this region.

The timescale of the collision between the 50 and 60 km s^{-1} clouds in G49.4−0.3 can be estimated as 0.2–0.6 Myr by assuming a collision length ranging from the width of the filamentary structure, ∼2 pc, to the full extension of the H II regions in G49.4−0.3, ∼6 pc. On the other hand, as we found no plausible evidence of physical association between the 68 km s^{-1} cloud and the H II regions in G49.4−0.3, it may be that the 60 and 68 km s^{-1} clouds are in the beginning of a collision, and compressed dense gas is observed in C^{18}O as shown in figure 14a.

In G49.57−0.27, the V-shaped gas distribution in the l–v diagram in figure 15b may also be interpreted as expansion of the H II region. However, as the radius of G49.57−0.27, ∼1.2 pc (table 1), is much smaller than that of the 50 km s^{-1} component of 3–4 pc, the observed V-shaped gas distribution cannot be attributed to expansion of the H II region. It is therefore more likely that the V shape was formed through the CCC process. If we assume a collision angle relative to the line of sight of $\theta = 45^\circ$, the timescale required for the 50 km s^{-1} cloud to completely punch the 56 km s^{-1} cloud can be estimated as 3–4 pc/6 km s^{-1} ≈ 0.5–0.7 Myr. Although we could not determine an accurate value of θ from position–position-velocity data of molecular clouds, $\theta = 45^\circ$ is a convenient solution as a first approximation of the angle of two colliding clouds (the error of <5 times is within the range of 86%).

Meanwhile, it is difficult to identify a CCC event in position–position-velocity data when the collision angle is parallel to the sky plane, and thus there may be unidentified CCCs in W 51 A. The fraction of such unidentified CCC events with collision angle of >80° is estimated to be less than 20%, if we tentatively assume that the cloud motions are all random (see appendix 5). To discuss these unidentified CCC events, we need to conduct a statistical study of CCCs in the Galaxy.

4.3 Massive star formation triggered by CCCs in W 51 A

G49.5−0.4 also includes relatively evolved H II regions with ages of a few Myrs, i.e., G49.5−0.4f, g, h, and i (table 1). As summarized at the beginning of subsection 4.2, the remnant CO components of these H II regions are found in the 50, 56, and 60 km s^{-1} clouds. These observed signatures can be interpreted as a CCC scenario or expansion of the H II regions. In the evolved H II regions, complementary distributions and bridge features are dissipated and cannot be observed. Therefore, in G49.5−0.4f, g, h, and i, it is difficult to conclude whether the exciting massive stars in these H II regions were formed via CCCs or not. If we tentatively assume that these H II regions were also formed via collisions among these three clouds, the collisions should have occurred since a few Myrs ago. The sequential collisions and star formation from the north to the south are consistent with the discussion of Okumura et al. (2001).

In G49.4−0.3, the figures derived in subsection 4.2 are consistent with the estimated ages of the H II regions (table 1), implying a scenario that the collision triggered formation of massive stars. In G49.57−0.27, the collision timescale of 0.5–0.7 Myr derived in subsection 4.2 is also consistent with the estimated age of the H II region of G49.57−0.27, 0.7 Myr (table 1). As the broad bridge feature indicates that the collision is still continuing, the collision in G49.57−0.27 is likely in the middle, which is consistent with the young age of G49.57−0.27.

Summarizing the discussions in subsections 4.1 and 4.2, the observational signatures of CCCs in G49.5−0.4, G49.4−0.3, and G49.57−0.27 represent collisions which have started since a few 0.1 Myr ago. This indicates that the four velocity components in this region, i.e., the 50, 56, 60, and 68 km s^{-1} clouds, are currently distributed close to each other, and are partly blended into one single molecular cloud as shown in figures 16a and 16b, which show the ^{13}CO (J = 1–0) and C^{18}O (J = 1–0) emissions, respectively, of the four clouds. Also, figures 17c and 17d show schematic pictures of the ^{13}CO (J = 1–0) distributions in W 51 A based on Ginsburg et al. (2015) as viewed from the Galactic north pole and the Galactic eastern side, respectively.

This is against the assumption of Okumura et al. (2001) that the four clouds are located in a line along the line of sight. However, in the latter evolutionary stage of their "pileup" scenario, it can be expected that the four clouds are completely merged into a single cloud (see figure 5 of Okumura et al. 2001). In this sense, our results are consistent with their CCC scenario.

In table 4, we compare the properties of the colliding molecular clouds in W 51 A with those of the other H II regions containing more than ten O-stars formed by CCC discussed in previous studies. The numbers of O-stars in G49.5−0.4 and G49.4−0.3 are roughly comparable with those in Westerlund 2, NGC 3603, and RCW 38. Furthermore, the H_2 column density of each of the larger clouds is also roughly comparable (1–3 × 10^{23} cm^{-2}). However, the molecular mass of the larger cloud in RCW 38 is significantly smaller than that of the other regions. The number of O-stars formed by CCCs possibly depends on H_2 column densities rather than molecular masses. The molecular clouds in G49.57−0.27 could not form O-stars because the H_2 column density is low. On the other hand, we cannot discuss the relationship between relative line-of-sight velocity separations and the number of O-stars from these data because of a large ambiguity in the three-dimensional colliding velocity. Figures 18a–18c show the correlations between the numbers of O-stars and the parameters of the molecular cloud in the H II regions listed in table 4. As mentioned above, the correlation between $N_{\rm max}(H_2)$ and the number of O-stars (figure 18b) is likely stronger than that between the molecular mass and the number of O-stars (figure 18a). In addition, there may also be a stronger positive correlation between the number of O-stars and the relative line-of-sight velocity (figure 18c). To establish a quantitative scenario for forming massive

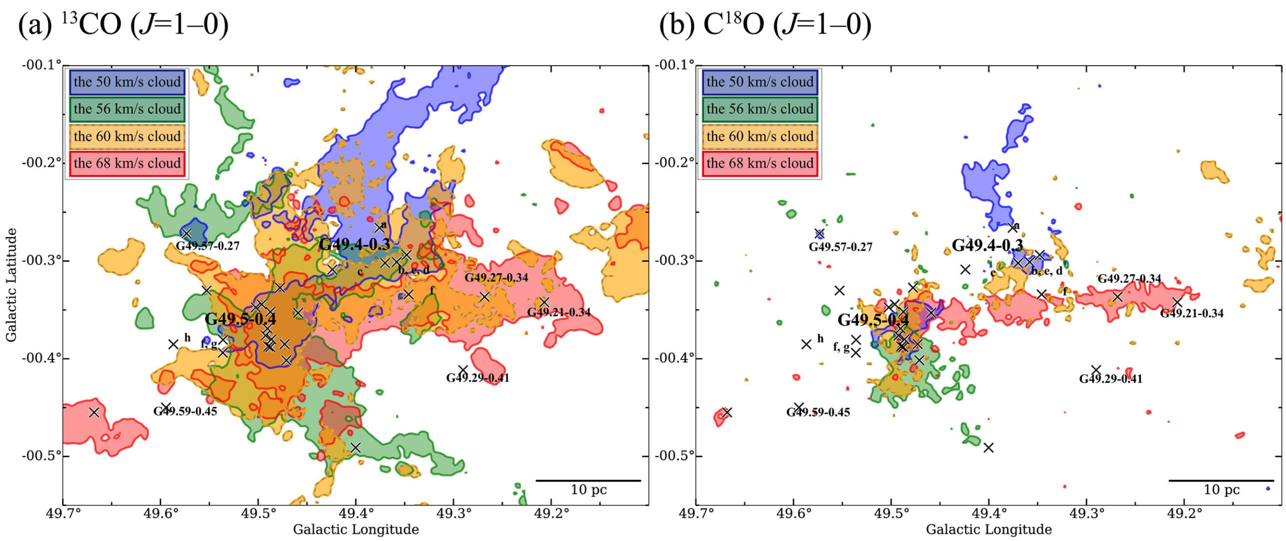

Fig. 16. (a) ^{13}CO ($J = 1$–0) integrated intensity distributions of the 50 (blue contour), 56 (green contour), 60 (orange contour with gray dashed contour), and 68 km s^{-1} clouds (red contour). The integration ranges are as in figure 6, and the contour levels are 10, 10, 10, and 8 K km s^{-1}, respectively. The crosses represent H II regions listed by Mehringer (1994). (b) As panel (a), but for the C^{18}O ($J = 1$–0) integrated intensity distributions.

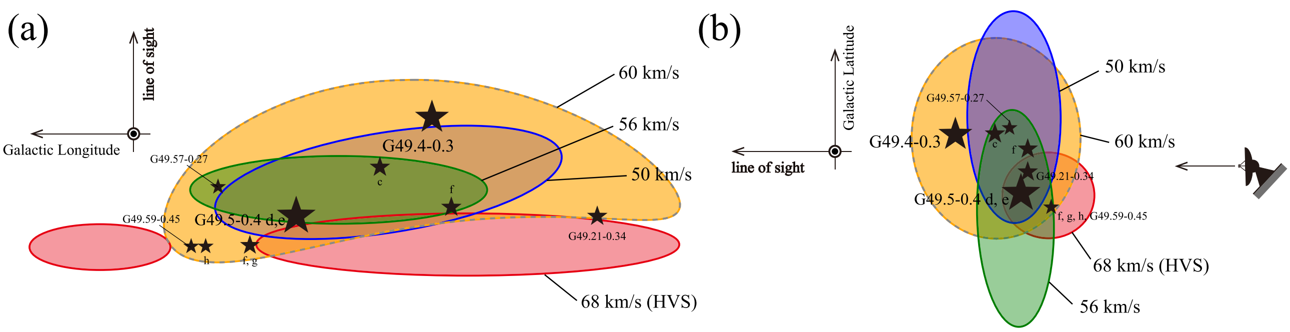

Fig. 17. (a) Schematic pictures of the distributions of the molecular gas in W 51 A based on Ginsburg et al. (2015) as viewed from the Galactic north pole. The star markers indicate the positions of the representative H II regions in W 51 A. (b) As panel (a), but as viewed from the Galactic eastern side.

stars via CCC, more studies, such as statistical studies and simulational studies, are required.

5 Summary

We carried out new ^{12}CO ($J = 1$–0), ^{13}CO ($J = 1$–0), and C^{18}O ($J = 1$–0) observations toward W 51 A as part of the FUGIN project with the Nobeyama 45 m telescope. These observations covered a large area of W 51 A (1$^\circ\!\!.$4 × 1$^\circ\!\!.$0) at an angular resolution of 20″ (∼0.5 pc). The main conclusions of the present study are summarized as follows:

(1) Our CO data identified four discrete velocity clouds with sizes and masses of ∼30 pc and 1.0–1.9 × 10^5 $M_\odot$ at radial velocities of 50, 56, 60, and 68 km s^{-1} in W 51 A. These four clouds mainly consist of the bright CO emissions toward the two bright H II region complexes G49.5−0.4 and G49.4−0.3 attached with filament hub structures elongated for several tens pc.

(2) Based on comparisons between our ^{13}CO ($J = 1$–0) data and the archival JCMT ^{13}CO ($J = 3$–2) data, it was revealed that all four clouds are physically associated with G49.5−0.4, while three of the four, i.e., the 50, 60, and 68 km s^{-1} clouds, interact with G49.4−0.3, as the ^{13}CO ($J = 3$–2)/^{13}CO ($J = 1$–0) intensity ratios in these clouds are higher than 1.0 near the H II regions. The LVG calculations indicate that such high ratios can be attributed to high-temperature gas heated by the massive stars in these regions. We also found that the isolated H II region G49.57−0.27 located ∼15 pc north of G49.5−0.4 is associated with the 50 and 56 km s^{-1} clouds.

(3) In each of these three H II regions, G49.4−0.5, G49.4−0.3, and G49.25−0.27, we revealed that the multiple velocity components associated with the H II

Table 4. Physical properties of molecular clouds toward H II regions formed by cloud–cloud collisions.*

Name (1)	Molecular masses ($M_\odot$) (2)	$N_{max}(H_2)$ (cm^{-2}) (3)	Relative LOS velocities ($km\,s^{-1}$) (4)	Age (Myr) (5)	Number of O-stars (6)	References (7)
G49.5−0.4	$\sim 4 \times 10^4$	9×10^{22}	6–20	∼0.1–2.6	28	This study, [1]
	$\sim 1 \times 10^5$	3×10^{23}				
	$\sim 1 \times 10^5$	2×10^{23}				
	$\sim 1 \times 10^5$	7×10^{22}				
G49.4−0.3	$\sim 8 \times 10^4$	1×10^{23}	10	∼0.1–0.8	∼6	This study, [1]
	$\sim 9 \times 10^4$	4×10^{22}				
G49.57−0.27	$\sim 1 \times 10^4$	3×10^{22}	6	∼0.7	0 (1 B0-star)	This study, [1]
	$\sim 4 \times 10^3$	3×10^{22}				
Westerlund 2	9×10^4	2×10^{23}	16	∼2.0	14	[2], [3]
	8×10^4	2×10^{22}				
NGC 3603	7×10^4	1×10^{23}	15	∼2.0	∼30	[4]
	1×10^4	1×10^{22}				
RCW 38	2×10^4	1×10^{23}	12	∼0.1	∼20	[5]
	3×10^3	1×10^{22}				

* (1) Name of H II regions. (2) Molecular mass derived from the ^{12}CO ($J = 1$–0) and ^{13}CO ($J = 1$–0) data by assuming LTE. (3) Maximum H_2 column density derived from the ^{12}CO ($J = 1$–0) and ^{13}CO ($J = 1$–0) data by assuming LTE. (4) Relative line-of-sight velocity separation among the colliding clouds. (5) Age of H II regions. (6) Number of O-stars. (7) References: [1] Okumura et al. (2000); [2] Furukawa et al. (2009); [3] Ohama et al. (2010); [4] Fukui et al. (2014); [5] Fukui et al. (2016).

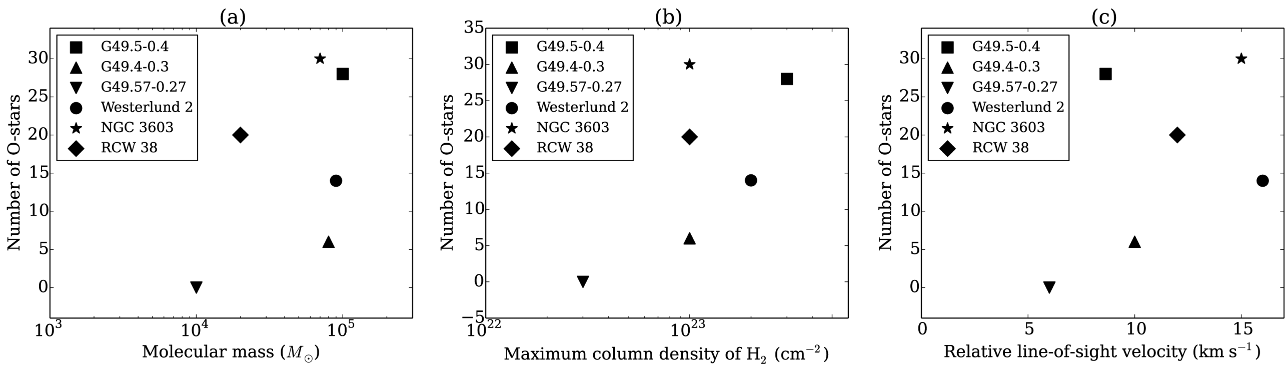

Fig. 18. Correlation between (a) the molecular mass and the number of O-stars, (b) $N_{max}(H_2)$ and the number of O-stars, and (c) the relative line-of-sight velocity and the number of O-stars. In panels (a) and (b), the molecular masses and $N_{max}(H_2)$ for the largest cloud in each H II region are plotted. In panel (c), the geometric mean of the relative velocities is plotted for G49.5−0.4.

regions show "spatially complementary distributions" on the sky and "broad bridge features" in the position–velocity diagrams. In particular, in G49.25−0.27 a combination of the complementary distribution and the bridge features represent a "V-shaped" gas distribution in the position–velocity diagram. These signatures have been discussed as observational signatures of CCC in recent theoretical and observational studies in Galactic H II regions.

(4) We estimated the timescales of the collisions in these three regions to be several 0.1 Myr by calculating crossing times of the collisions. These estimates are consistent with the ages of the H II regions measured from the sizes of the H II regions with the 21 cm continuum map.

(5) Our present results lend more credence to a CCC scenario in W 51 A whereby multiple velocity components have been continuously colliding with each other, resulting in active massive star formation in W 51 A.

(6) On the other hand, our results are also consistent with the discussion by Carpenter and Sanders (1998) that the 50, 56, and 60 km s^{-1} clouds represent kinematic structure within a single molecular cloud, as the total molecular mass in W 51 is consistent with its virial mass at a 100 pc scale, suggesting that self-gravity will play a critical role in the evolution of the molecular clouds in

W 51. To fully understand the kinematics and interactions of molecular clouds in W 51, which will allow us to investigate the future of this region, it is important to study W 51 B using the same CO dataset. We will work on this issue in a separate paper.

Acknowledgments

This study was financially supported by Grants-in-Aid for Scientific Research (KAKENHI) of the Japanese Society for the Promotion of Science (JSPS; grant numbers 15K17607, 17H06740, and 18K13580). The authors would like to thank all the members of the 45 m group of Nobeyama Radio Observatory for support during the observation. Data analysis was carried out on the open use data analysis computer system at the Astronomy Data Center (ADC) of the National Astronomical Observatory of Japan (NAOJ), and made use of Astropy, a community-developed core Python package for astronomy (Astropy Collaboration et al. 2013); APLpy, an open-source plotting package for Python (Robitaille & Bressert 2012); astrodendro, a Python package to compute dendrograms of astronomical data (Rosolowsky et al. 2008); and SCIMES, a Python package to find relevant structures in dendrograms of molecular gas emission using the spectral clustering approach (Colombo et al. 2015). The authors would also like to thank NASA, National Radio Astronomy Observatory (NRAO), and Dr. H. Parsons for providing FITS data from the Spitzer Space Telescope and JCMT, and VGPS, respectively.

Appendix 1 Velocity channel maps of the CO (J = 1–0) emissions

In figures 19a–19c we present velocity channel maps of the ^{12}CO (J = 1–0), ^{13}CO (J = 1–0), and C^{18}O (J = 1–0) emissions at a velocity step of 3.25 km s^{-1}.

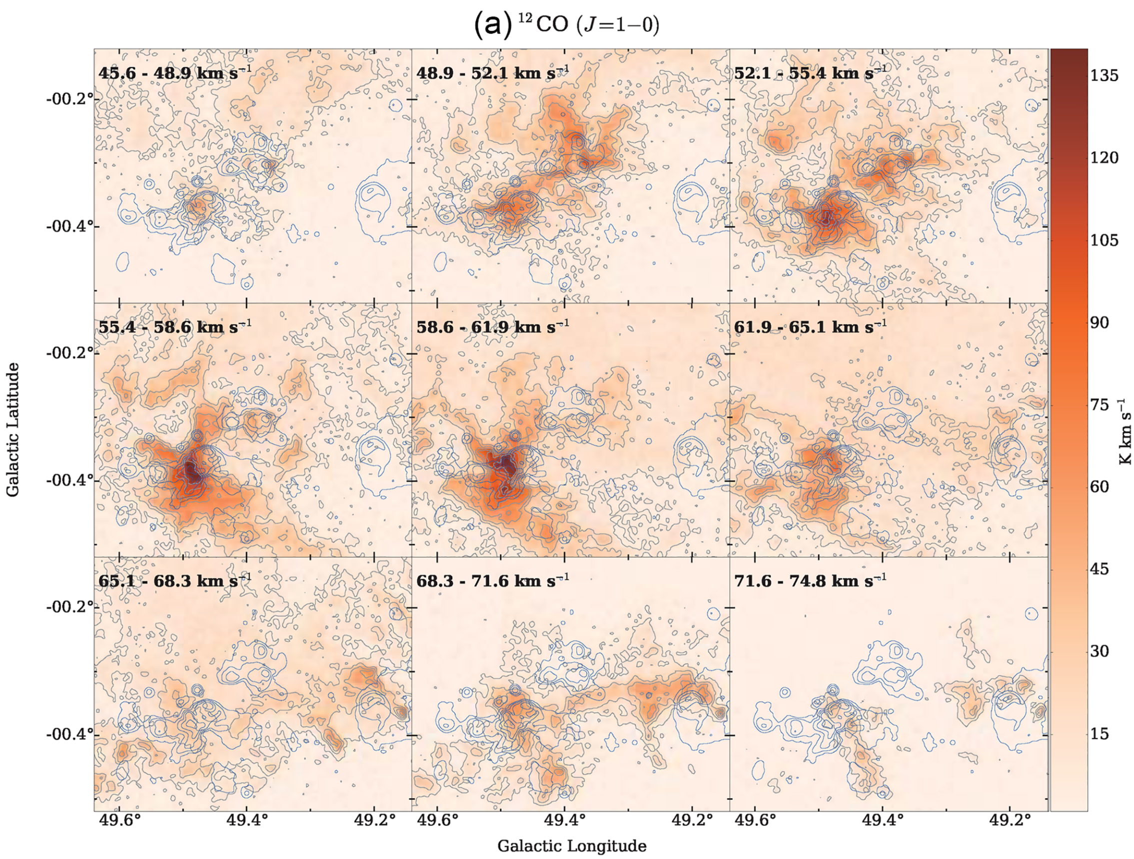

Fig. 19. (a) Velocity channel maps of the ^{12}CO (J = 1–0) emissions. The gray contours are plotted with 8σ (16 K km s^{-1}) intervals starting from the 4σ (8 K km s^{-1}) level. The integration range in each panel is presented in the top-left corner of the panel. The blue contours indicate the THOR 21 cm radio continuum emission combined with the VGPS data (Stil et al. 2006; Beuther et al. 2016), and are plotted from 0.03 (dashed lines) to 3.0 Jy sr^{-1} with logarithmic steps. The angular resolution of the THOR data combined with VGPS is 25″. (b) As panel (a) but for ^{13}CO (J = 1–0). The gray contours are plotted with 8σ (8 K km s^{-1}) intervals starting from the 4σ (4 K km s^{-1}) level. (c) As panel (a) but for C^{18}O (J = 1–0). The gray contours are plotted with 3σ (3 K km s^{-1}) intervals starting from the 3σ (3 K km s^{-1}) level.

(b) ^{13}CO (J=1–0)

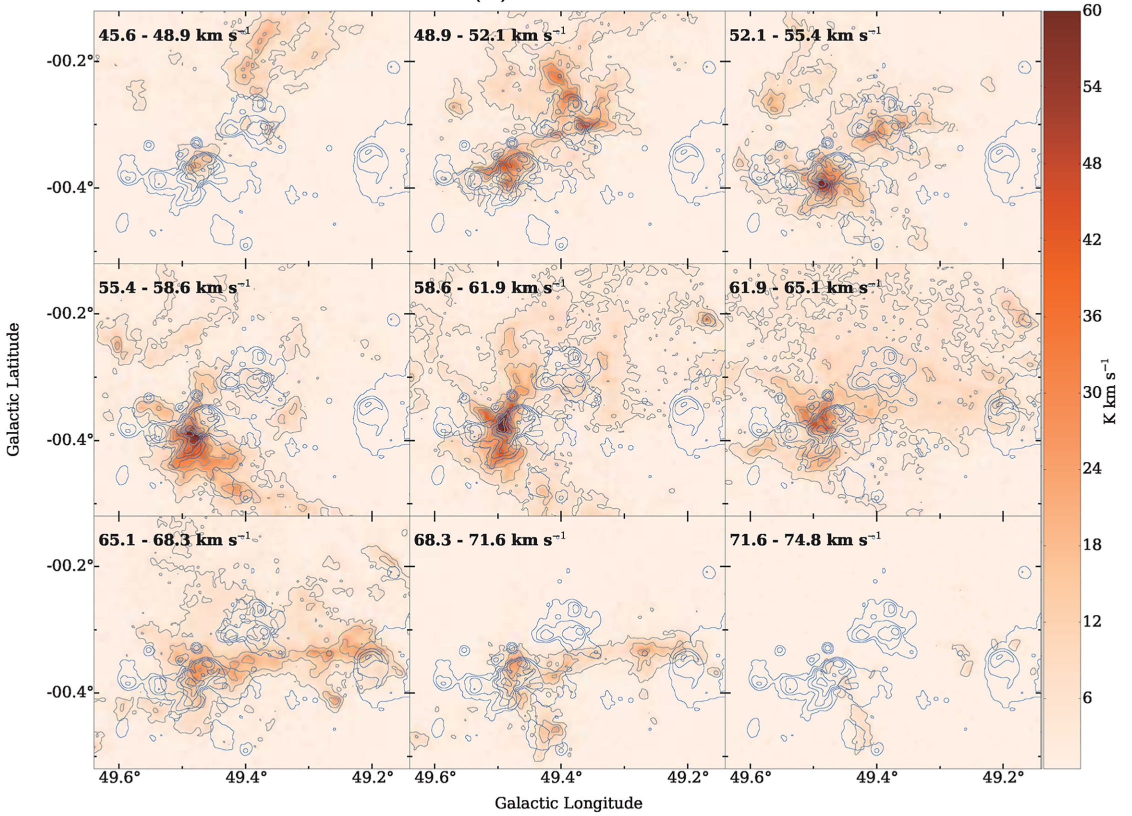

(c) C^{18}O (J=1–0)

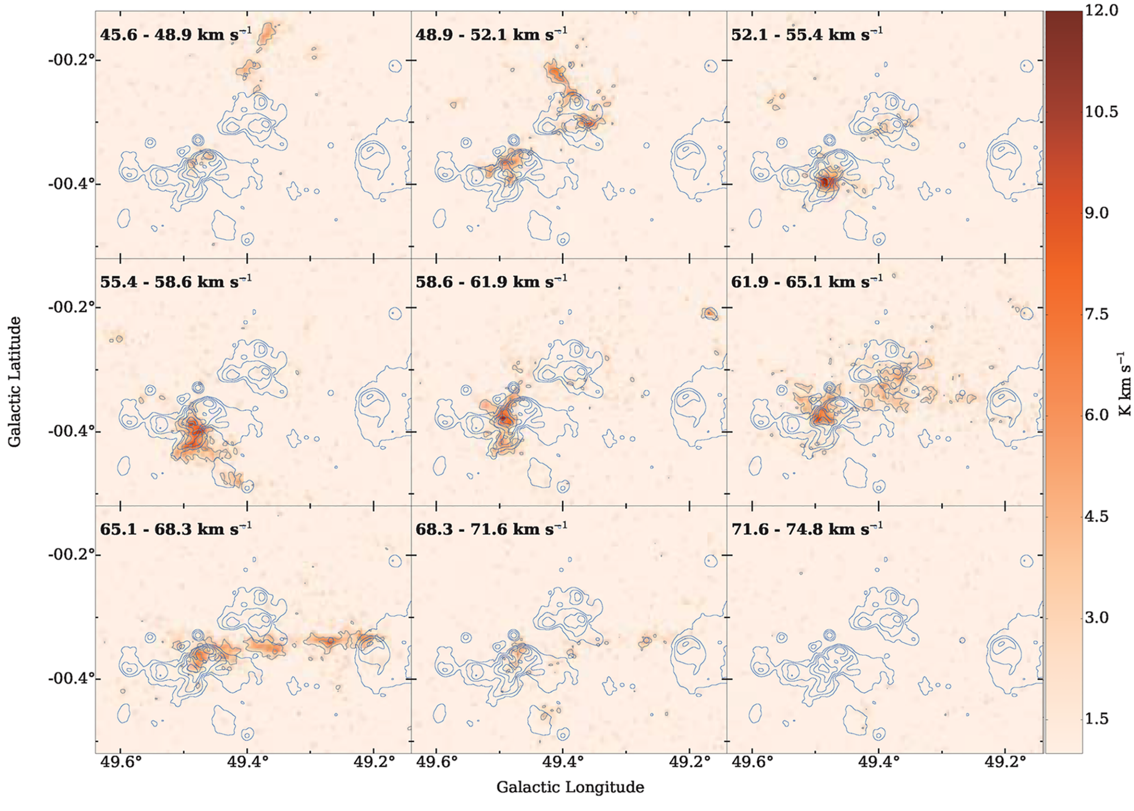

Fig. 19 (Continued).

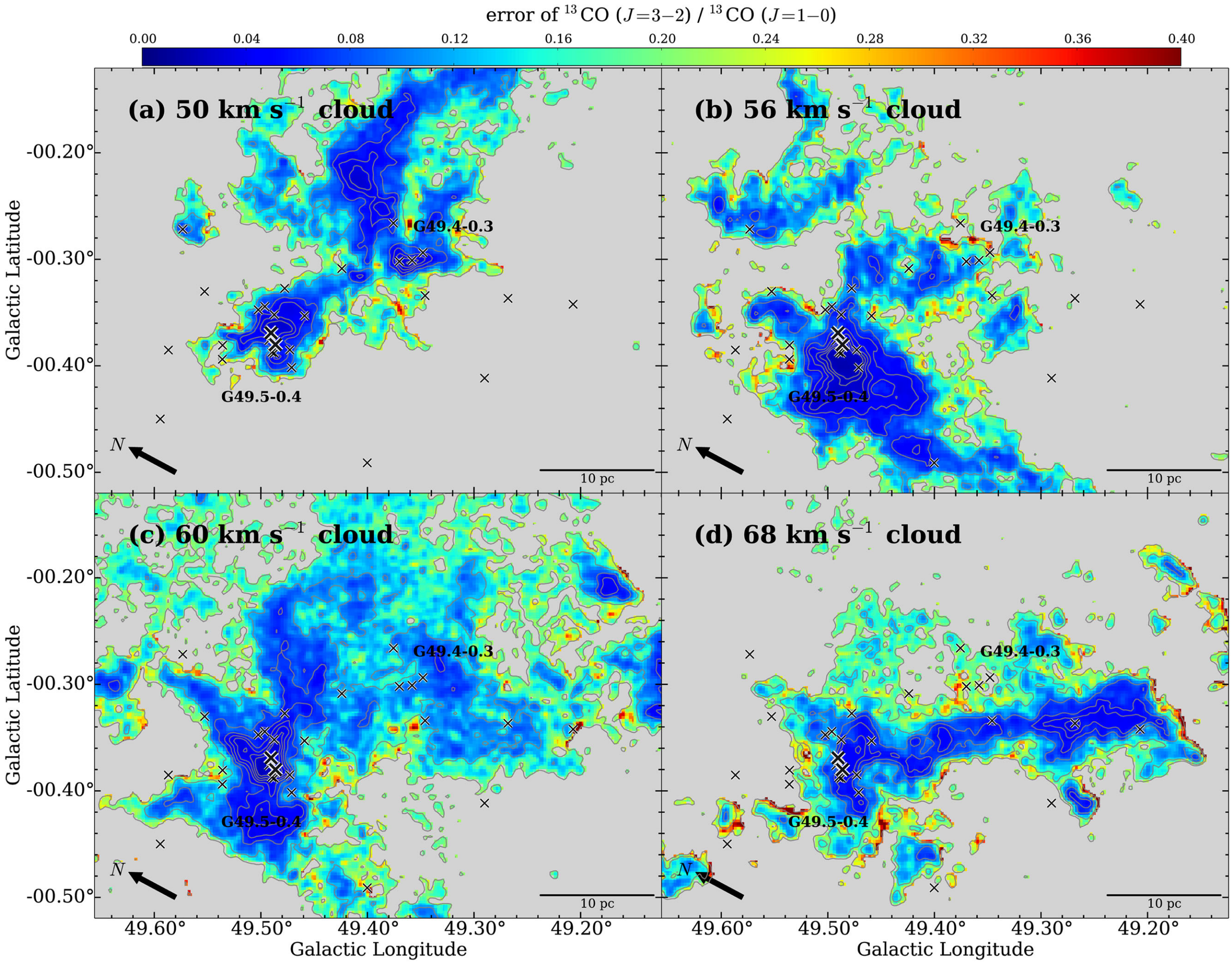

Fig. 20 Map of the error associated with R^{13}_{3210} (figure 8a–8d) for each pixel. The errors were estimated from the calibration error of the ^{13}CO (J = 1–0) and ^{13}CO (J = 3–2) data (15% and 10%, respectively).

Appendix 2 Errors associated with R^{13}_{3210}

Figure 20 presents a map of the error associated with R^{13}_{3210} for each pixel.

Appendix 3 Large velocity gradient analysis

To investigate high-temperature gas in the molecular clouds of W 51 A, we utilize large velocity gradient (LVG) calculations (e.g., Goldreich & Kwan 1974). The assumption of a uniform velocity gradient is not always valid in the molecular gas associated with H II regions. However, radiative transfer calculations assuming a microturbulent cloud interacting with an H II region shows no significant difference from the LVG analysis (e.g., Leung & Liszt 1976; White 1977). We therefore adopt the LVG approximation in the present study. We adopted here the abundance ratio of [^{12}CO]/[^{13}CO] = 77 (Wilson & Rood 1994) and the fractional CO abundance X(CO) = [^{12}CO]/[H_2] = 10^{-4} (e.g., Frerking et al. 1982; Leung et al. 1984). Two velocity gradients dv/dr of 5 and 10 km s^{-1} pc^{-1} were adopted, by assuming a typical velocity width of individual velocity clouds, ~3 km s^{-1}, and a full velocity width of the four velocity clouds, ~30 km s^{-1} (see figure 4), multiplied by a typical size of the molecular gas components of ~3 pc.

Figure 21 shows R^{13}_{3210} distributions calculated with LVG for different densities $n(H_2)$ as a function of kinetic temperature T_k of gas, indicating that R^{13}_{3210} is sensitive to gas temperature. In all the $n(H_2)$ cases, R^{13}_{3210} of higher than 1.0 corresponds to T_k of higher than ~20 K, which is significantly higher than the typical temperature of molecular clouds without star formation, 10 K (Fukui et al. 2016).

Appendix 4 H_2 column density derived from ^{12}CO ($J = 1$–0) and $C^{18}O$ ($J = 1$–0) emissions

Figure 22 shows the column density of H_2 molecules derived from the ^{12}CO ($J = 1$–0) and $C^{18}O$ ($J = 1$–0) emissions for all four clouds.

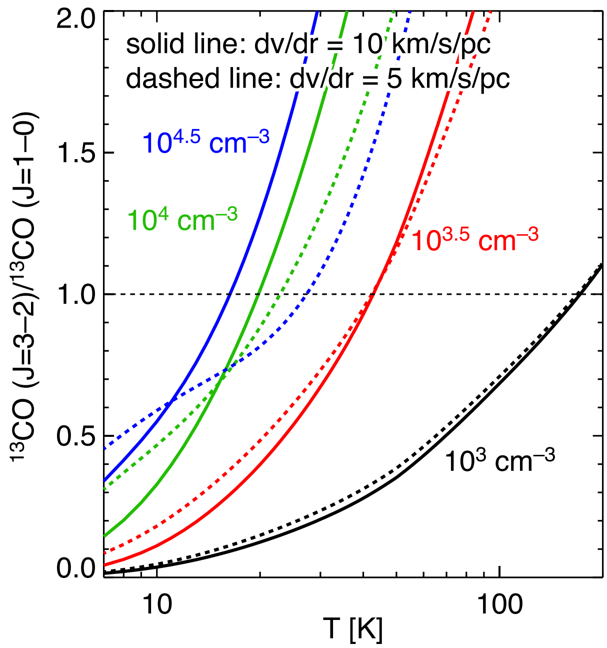

Fig. 21 Curves of R^{13}_{3210} as a function of T_k and $n(H_2)$, estimated using the LVG calculations. dv/dr is assumed to be 10 km s^{-1} pc^{-1} (solid lines) and 5 km s^{-1} pc^{-1} (dashed lines).

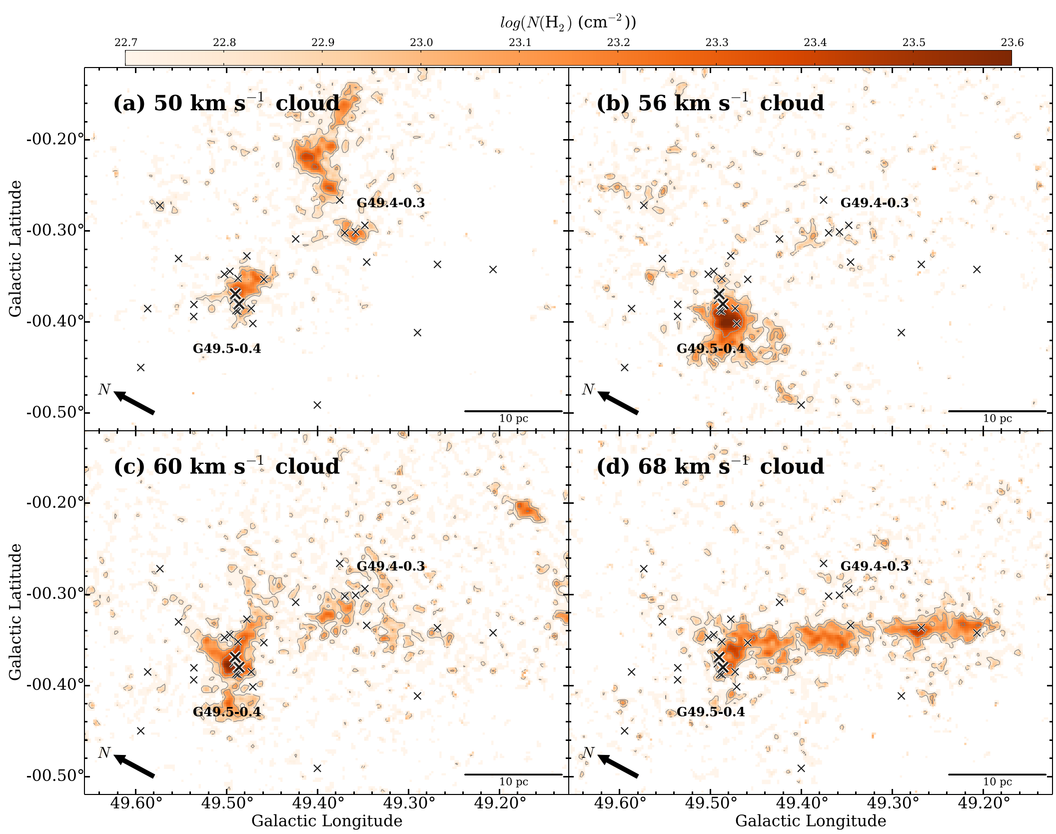

Fig. 22 Column density of H_2 molecules derived from the ^{12}CO ($J = 1$–0) and $C^{18}O$ ($J = 1$–0) emissions of the (a) 50, (b) 56, (c) 60, and (d) 68 km s^{-1} clouds, with integration ranges of 46.9–52.1, 52.8–58.6, 59.3–64.5, and 65.1–71.0 km s^{-1}, respectively. The gray contours are plotted with 6 × 10^{22} cm^{-2}, 1 × 10^{23} cm^{-2}, and 2 × 10^{23} cm^{-2} level. The crosses represent H II regions listed by Mehringer (1994).

Appendix 5 Fraction of the collision angle with random motion

Figure 23 shows the normalized probability of collision angle θ ($0^\circ \le \theta \le 90^\circ$) and its cumulative fraction when we assume that the motions of the colliding clouds are random. The normalized probability is relative to $\sin\theta$, and thus its cumulative fraction is $1 - \cos\theta$.

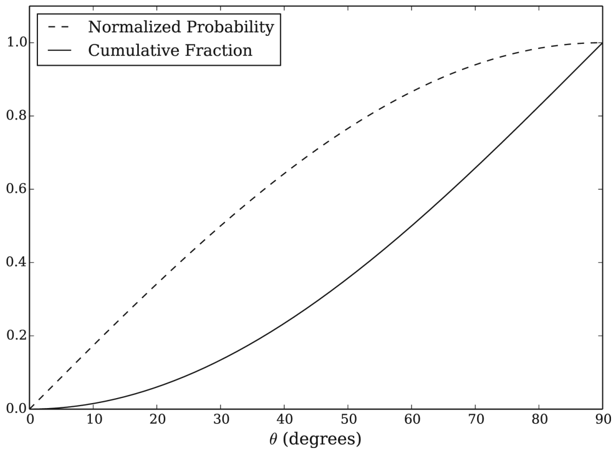

Fig. 23 The dashed curve and solid curve show the normalized probability of collision angle θ ($0^\circ \le \theta \le 90^\circ$) and its cumulative fraction, respectively, when we assume that the motions of the colliding clouds are random. $\theta = 0^\circ$ means that the collision angle is parallel to the line of sight.

References

Anathpindika, S. V. 2010, MNRAS, 405, 1431
Anderson, L. D., Bania, T. M., Balser, D. S., Cunningham, V., Wenger, T. V., Johnstone, B. M., & Armentrout, W. P. 2014, ApJS, 212, 1
Arnal, E. M., & Goss, W. M. 1985, A&A, 145, 369
Astropy Collaboration 2013, A&A, 558, A33
Beuther, H., et al. 2016, A&A, 595, A32
Bieging, J. 1975, in H II Regions and Related Topics, ed. T. L. Wilson & D. Downes (Berlin: Springer-Verlag), 443
Bonnell, I. A., Bate, M. R., Clarke, C. J., & Pringle, J. E. 2001, MNRAS, 323, 785
Burton, W. B., & Shane, W. W. 1970, in IAU Symp. 38, The Spiral Structure of our Galaxy, ed. W. Becker & K. Georgios Ioannou (Dordrecht: Reidel), 397
Cardelli, J. A., Clayton, G. C., & Mathis, J. S. 1989, ApJ, 345, 245
Carey, S. J., et al. 2009, PASP, 121, 76
Carpenter, J. M., & Sanders, D. B. 1998, AJ, 116, 1856
Colombo, D., Rosolowsky, E., Ginsburg, A., Duarte-Cabral, A., & Hughes, A. 2015, MNRAS, 454, 2067
Dickman, R. L. 1978, ApJS, 37, 407
Frerking, M. A., Langer, W. D., & Wilson, R. W. 1982, ApJ, 262, 590
Fujita, S., et al. 2021, PASJ, 73, S273
Fukui, Y., et al. 2014, ApJ, 780, 36
Fukui, Y., et al. 2015, ApJ, 807, L4
Fukui, Y., et al. 2016, ApJ, 820, 26
Fukui, Y., et al. 2018a, ApJ, 859, 166
Fukui, Y., et al. 2018b, PASJ, 70, S44
Fukui, Y., Tsuge, K., Sano, H., Bekki, K., Yozin, C., Tachihara, K., & Inoue, T. 2017, PASJ, 69, L5
Furukawa, N., Dawson, J. R., Ohama, A., Kawamura, A., Mizuno, N., Onishi, T., & Fukui, Y. 2009, ApJ, 696, L115
Ginsburg, A., Bally, J., Battersby, C., Youngblood, A., Darling, J., Rosolowsky, E., Arce, H., & Lebrón Santos, M. E. 2015, A&A, 573, A106
Goldreich, P., & Kwan, J. 1974, ApJ, 189, 441
Habe, A., & Ohta, K. 1992, PASJ, 44, 203
Haworth, T. J., et al. 2015a, MNRAS, 450, 10
Haworth, T. J., Shima, K., Tasker, E. J., Fukui, Y., Torii, K., Dale, J. E., Takahira, K., & Habe, A. 2015b, MNRAS, 454, 1634
Hayashi, K., et al. 2018, PASJ, 70, S48
Indebetouw, R., et al. 2005, ApJ, 619, 931
Inoue, T., & Fukui, Y. 2013, ApJ, 774, L31
Inoue, T., Hennebelle, P., Fukui, Y., Matsumoto, T., Iwasaki, K., & Inutsuka, S. 2018, PASJ, 70, S53
Kang, M., Bieging, J. H., Kulesa, C. A., Lee, Y., Choi, M., & Peters, W. L. 2010, ApJS, 190, 58
Kang, M., Bieging, J. H., Povich, M. S., & Lee, Y. 2009, ApJ, 706, 83
Kawamura, A., Onishi, T., Yonekura, Y., Dobashi, K., Mizuno, A., Ogawa, H., & Fukui, Y. 1998, ApJS, 117, 387
Kim, H., Nakajima, Y., Sung, H., Moon, D.-S., & Koo, B.-C. 2007, J. Korean Astron. Soc., 40, 17
Kobayashi, M. I. N., Kobayashi, H., Inutsuka, S., & Fukui, Y. 2018, PASJ, 70, S59
Kohno, M., et al. 2018, PASJ, 70, S50
Koo, B.-C. 1997, ApJS, 108, 489
Koo, B.-C. 1999, ApJ, 518, 760
Koo, B.-C., & Moon, D.-S. 1997a, ApJ, 475, 194
Koo, B.-C., & Moon, D.-S. 1997b, ApJ, 485, 263
Krumholz, M. R., Klein, R. I., McKee, C. F., Offner, S. S. R., & Cunningham, A. J. 2009, Science, 323, 754
Kumar, M. S. N., Kamath, U. S., & Davis, C. J. 2004, MNRAS, 353, 1025
Kuno, N., et al. 2011, in Proc. 2011 XXXth URSI General Assembly and Scientific Symposium, Vol. 1 (New York: IEEE), 3670
Leung, C. M., Herbst, E., & Huebner, W. F. 1984, ApJS, 56, 231
Leung, C.-M., & Liszt, H. S. 1976, ApJ, 208, 732
Makai, Z., Anderson, L. D., Mascoop, J. L., & Johnstone, B. 2017, ApJ, 846, 64
Mehringer, D. M. 1994, ApJS, 91, 713
Minamidani, T., et al. 2016, SPIE Proc., 9914, 99141Z
Nishimura, A., et al. 2017, arXiv:1706.06002
Nishimura, A., et al. 2018, PASJ, 70, S42
Ohama, A., et al. 2010, ApJ, 709, 975
Ohama, A., et al. 2018a, PASJ, 70, S47
Ohama, A., et al. 2018b, PASJ, submitted (arXiv:1706.05652)
Oka, T., Nagai, M., Kamegai, K., Tanaka, K., & Kuboi, N. 2007, PASJ, 59, 15
Okumura, S., Miyawaki, R., Sorai, K., Yamashita, T., & Hasegawa, T. 2001, PASJ, 53, 793

Okumura, S., Mori, A., Nishihara, E., Watanabe, E., & Yamashita, T. 2000, ApJ, 543, 799
Pankonin, V., Payne, H. E., & Terzian, Y. 1979, A&A, 75, 365
Parsons, H., Thompson, M. A., Clark, J. S., & Chrysostomou, A. 2012, MNRAS, 424, 1658
Rengarajan, T. N., Cheung, L. H., Fazio, G. G., Shivanandan, K., & McBreen, B. 1984, ApJ, 286, 573
Robitaille, T., & Bressert, E. 2012, Astrophysics Source Code Library, ascl:1208.017
Rosolowsky, E. W., Pineda, J. E., Kauffmann, J., & Goodman, A. A. 2008, ApJ, 679, 1338
Sano, H., et al. 2018, PASJ, 70, S43
Saral, G., et al. 2017, ApJ, 839, 108
Sato, M., Reid, M. J., Brunthaler, A., & Menten, K. M. 2010, ApJ, 720, 1055
Shetty, R., Glover, S. C., Dullemond, C. P., & Klessen, R. S. 2011, MNRAS, 412, 1686
Shimoikura, T., et al. 2013, ApJ, 768, 72
Spitzer, L., Jr. 1978, Physical Processes in the Interstellar Medium (New York: John Wiley & Sons)
Stil, J. M., et al. 2006, AJ, 132, 1158
Takahira, K., Shima, K., Habe, A., & Tasker, E. J. 2018, PASJ, 70, S58
Takahira, K., Tasker, E. J., & Habe, A. 2014, ApJ, 792, 63
Tan, J. C., Beltran, M. T., Caselli, P., Fontani, F., Fuente, A., Krumholz, M. R., McKee, C. F., & Stolte, A. 2014, in Protostars and Planets VI, ed. H. Beuther et al. (Tuscon, AZ: University Arizona Press), 149
Torii, K., et al. 2011, ApJ, 738, 46
Torii, K., et al. 2015, ApJ, 806, 7
Torii, K., et al. 2017, ApJ, 835, 142
Torii, K., et al. 2021, PASJ, 73, S368
Tsuboi, M., Miyazaki, A., & Uehara, K. 2015, PASJ, 67, 109
Umemoto, T., et al. 2017, PASJ, 69, 78
Westerhout, G. 1958, Bull. Astron. Inst. Netherlands, 14, 215
White, R. E. 1977, ApJ, 211, 744
Wilson, T. L., & Rood, R. 1994, ARA&A, 32, 191
Wolfire, M. G., & Cassinelli, J. P. 1987, ApJ, 319, 850
Wynn-Williams, C. G., Becklin, E. E., & Neugebauer, G. 1974, ApJ, 187, 473
Zinnecker, H., & Yorke, H. W. 2007, ARA&A, 45, 481